MEASUREMENT OF DIRECT LEPTON PRODUCTION AT HIGH TRANSVERSE MOMENTUM IN PROTON-NUCLEUS INTERACTIONS

JAMES J. MUELLER

A DISSERTATION

PRESENTED TO THE

FACULTY OF PRINCETON UNIVERSITY

IN CANDIDACY FOR THE DEGREE

OF DOCTOR OF PHILOSPHY

RECOMMENDED FOR ACCEPTANCE BY THE

DEPARTMENT OF

PHYSICS

October 1980

TABLE OF CONTENTS

ABSTRACT

We have measured the inclusive single muon yield from 200-, 300-, and 400 —GeV/c protons interacting in W, Cu, and Be targets for muon transverse momentum (P_T) between 1.5 and 5.8 GeV/c. The ratio of muon yield to the pion yield is approximately constant (1.5×10^{-4}) in the region $1.5<P_T<4.5$ and rises to a value of 3×10^{-4} at $P_T = 5.8$ GeV/c. The rise is consistent with an increasing contribution from continuum muon pairs. We find the muon yield at $P_T = 1.5$ GeV/c is consistent with a charm production cross-section of 20-30 μb per nucleon depending on the production model assumed. The data imply an upper limit for bottom particle production of approximately 200 nb per nucleon.

We report also on a measurement of the inclusive single electron yield from 400 GeV/c protons incident on a Be target at $P_T = 4.6$ GeV/c and a search for muons produced in coincidence with these electrons. No electron-muon coincidence signal was observed, which gives a 90% confidence upper limit for the ratio $e\mu/\mu\mu < .27$.

ACKNOWLEDGEMENTS

I acknowledge the large contributions of my fellow collaborators who made this experiment possible: Dikran Antreasyan, Jim Cronin, Henry Frisch, Louis Kluberg, Pierre Piroue, Mel Shochet, and Dick Sumner. I also thank the many people whose constant encouragement, occasional inspiration and subtle but unrelenting pressure made this thesis possible. Particular thanks go to my advisor, Pierre Piroue, who took me on as his thesis student during a somewhat awkward stage of the experiment and guided me through this adventure; to Richard Sumner and Louis Kluberg who taught me some of the tricks of the trade during my stint at Fermilab; and Bernard Pope for getting me back on the track and offering many suggestions to improve the drafts of this manuscript. Many thanks to my parents for always offering their support when needed. Special thanks to Colleen, my wife, for the million and one ways in which she helped, and made it all worthwhile.

CHAPTER 1

INTRODUCTION

Over the last decade "direct leptons" produced in hadronic collisions have attracted an increasing amount of experimental and theoretical attention. Two of the greatest experimental successes have been: (1) the discovery of new hadronic degrees of freedom through production of new vector mesons (Ψ and Υ families) and their subsequent decays into lepton pairs and (2) the use of lepton pair production in probing the constituent nature of hadrons. Testing of theoretical ideas at the basis of quantum chromodynamics has also been possible in the last few years as more dilepton data are collected over a wide kinematic range.

Direct leptons refer to all leptons which cannot be accounted for as decay products of well understood sources, such as π, K, and η. Possible sources of direct leptons can be conveniently classified into four categories:

(1) vector meson decays

$\phi, \rho, \omega, \Psi, \Upsilon, .. \rightarrow \mu^+ \mu^-$

(2) continuum dileptons produced through Drell-Yan mechanism.

$\gamma^* \rightarrow \mu^+ \mu^-$

(3) decays of heavy leptons

$\tau \rightarrow \mu \nu \bar{\nu}$

(4) semileptonic decays of heavier mesons with new quantum numbers(e.g. charm)

$D \rightarrow K \ell \nu$

The above list displays the wealth of physics one can attempt to investigate by measuring the inclusive production of single leptons and lepton pairs.

THE EXPERIMENT

In this experiment we extend a previous measurement of the single muon cross-section by our group (Chicago-Princeton group[9]) over a larger kinematic range and with increased statistical accuracy. We measure the inclusive cross-section:

$P + \text{Nucleus} \rightarrow \mu^{\pm} + X$ nucleus = Be, Cu, W

$1.5 < P_T < 6.16$ GeV/c , where P_T = transverse momentum of the $\mu^{\pm}$

$\sqrt{s}$ = 27.4, 24.3, 19.7 GeV , where s = C.M. energy squared

We can use these results to set upper limits on the production of various particles which decay into muons and also get information on the manner in which the parents of the muons are produced. In

addition we performed a measurement of the direct electron cross-section at a single transverse momentum,

$$P + Be \rightarrow e^- + X$$

$$P_T = 4.62 \text{ GeV/c}$$

$$\sqrt{s} = 27.4 \text{ GeV}$$

which provided an independent check of the muon measurement. At the same time we looked for muons coincident with these direct electrons in the same manner as was done in our measurement of dimuons[15]. Our apparatus was such that the $e\mu$ pair would have needed an invariant mass of at least 8 GeV/c^2 in order to have been observed. We obviously anticipated no $e\mu$ coincidences at such a high mass, as one would expect from conservation of lepton number, but the prior existence of the second arm of the spectrometer tempted us to include this measurment in our program. We draw on our measurement of dimuon production[1] only as it bears on the analysis of the above reactions. This topic is treated extensively in the thesis of D. Antreasyan (University of Chicago)[2].

HISTORICAL BACKGROUND

The first experiments designed to measure direct lepton yields in hadron collisions were performed in 1964 by a Columbia-BNL[3] group at Brookhaven National Laboratory and by a group at Argonne National Laboratory[4]. The motivation was to search for the hypothetical mediator of the weak interaction, W, by its decay

mode:

$$W \rightarrow \mu + \nu$$

An enhancement in the muon yield was expected at $P_T = M_W/2$. Although no appreciable signal was seen above the pion and kaon decay background, the basic technique pointed the way to further experimentation.

Their detection of direct muons relied on the use of a dense absorber placed between target and detectors. This absorber acted as a filter, attenuating hadrons and allowing the muons to pass through; thus shortening the decay path length of the hadrons.

Yamaguchi[5] pointed out that even if a signal had been seen, it might have not been due to the W but due to electromagnetic production, therefore the Brookhaven-Columbia[6] group went on to study the reaction :

$$P + \text{Nucleus} \rightarrow \mu^+ \mu^- + X$$

This experiment observed a continuum dimuon signal but no clear bumps were seen. Evident in the data was a broad shoulder which is now known to have been due to the production of the J/ψ resonance and its decay to a pair of muons. The results of these experiments led the way to the large amount of fruitful experimental activity in this field in recent years.

SINGLE LEPTONS

Single leptons, which had been reported by a Serpukhov group at the Fermilab conference(1972)[7], were first observed at Fermi National Accelerator Laboratory(F.N.A.L.) in 1974. This group(Chicago-Princeton)[8] observed single muons, a Columbia-F.N.A.L.[9] group observed single electrons,and the CCRS group at the ISR observed single electrons.[10]

The gross features of the data were surprising. The ratio l/π was observed to remain constant at a value of $l/\pi = 10^{-4}$, over a range of transverse momenta from 1 GeV/c to 5 GeV/c where the cross-sections fell by almost 6 orders of magnitude. The initial Chicago-Princeton results are displayed in figure 1-1. These data are a subset of the data sample analyzed in this thesis.

The origin of these leptons was, and to some extent still is, a subject of some controversy. Naively,the constancy of the ratio, l/π, would imply that the parents of the muons are produced by the same mechanism as pions. In this case the muon cross-section reflects the production dynamics of the hadronic parents. The single lepton yields appeared to be too large to be accommodated by the Drell-Yan model.[11] The Drell-Yan mechanism produces a continuum of dimuons by the annihilation of a point-like constituent in one nucleon with one in the other nucleon. A diagram of this process is shown in figure 1-2.

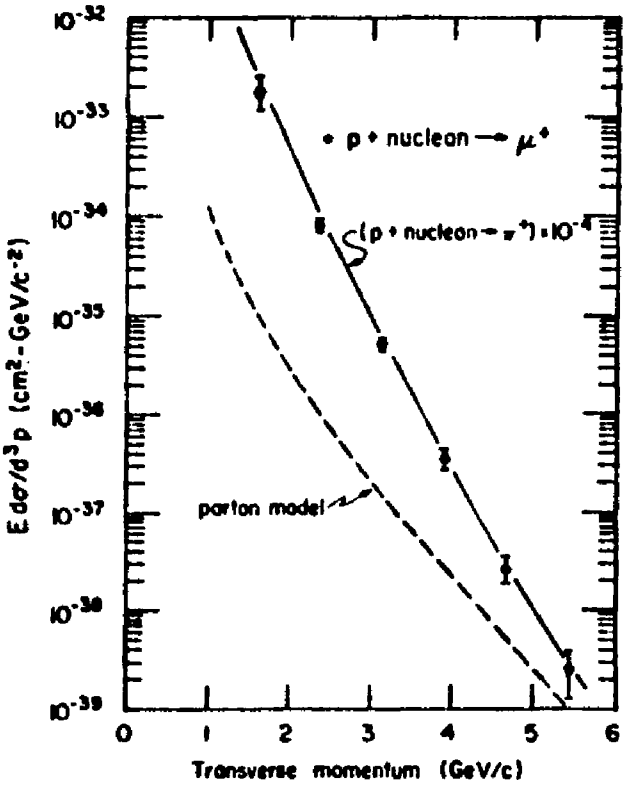
10^{-32}
10^{-33}
10^{-34}
10^{-35}
10^{-36}
10^{-37}
10^{-38}
10^{-39}
$E\,d\sigma/d^3p$ (cm²-GeV/c³)
• p + nucleon → μ^+
(p + nucleon → π^+) × 10^{-4}
parton model
0
1
2
3
4
5
6
Transverse momentum (GeV/c)

FIG. 1-1

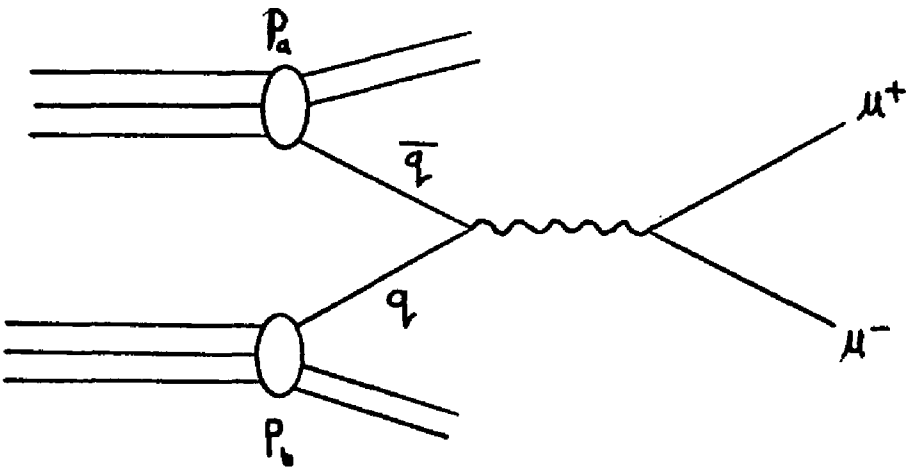
P_a
$\bar{q}$
μ^+
q
μ^-
P_b

FIG. 1-2

The most promising explanations attributed the single muon spectrum to contributions from various hadronic sources. Bourquin and Gaillard[12] devised one of the more successful models and asserted that a contribution from charmed mesons, in particular D and $\underline{D}$ decays, could account for the muon yield between 1 and 2 GeV/c transverse momentum.

More recently Brown et al. at F.N.A.L.[13] has observed single muons without a partner in the region around 1 GeV/c transverse momentum. The spectrometer has a very large acceptance for observing a second muon if one is present. They attribute these single muons to D meson decay and predict a total cross-section of 13 - 60 μB.

DIMUONS

In 1974 an extraordinarily narrow resonance, the J/Ψ[14], was observed in the reaction:

$$p + \text{NUCLEUS} \rightarrow \mu^+ \mu^- + X$$

at a dimuon invariant mass of 3.1 GEV. Its narrow width necessitated the introduction of a new quantum number, charm, to fit this particle into the present theories of strong interactions. The particle was interpreted as a bound state of a quark and antiquark of new flavor, charm. Examination of the dimuon invariant mass spectrum proved to be a very sensitive technique in searching for new hadronic degrees of freedom through decay of vector mesons into $\mu^+ \mu^-$. This technique again proved itself valuable in 1977 when another vector meson, the Υ, and its radial excitations were discovered.

In addition to the resonances, a continuum of dimuons exists. The continuum can be explained by the annihilation of the point-like constituents in the nucleon. The production cross-section has been shown to obey the following scaling relation[15]:

Furthermore, structure functions derived from this process are in agreement with results obtained in deep inelastic lepton-nucleon scattering[16].

CHAPTER 2

APPARATUS

The experiment was performed in the Proton East Area at F.N.A.L.. A proton beam, slowly extracted from the main accelerator, was delivered to a target viewed by an asymmetric double arm spectrometer (figure 2-1). The small aperture magnetic arm selects and identifies particles at 90° in the proton-nucleon center-of-mass, while the second arm, referred to as the Multi Hole Spectrometer (MHS), provides large solid angle detection of muons for which $P_T > 3.2$ GeV. The MHS is capable of only rough polar and azimuthal angle measurement.

The apparatus has evolved over a period of four years. The MHS was an addition to the spectrometer constructed in 1975. The results presented in this thesis utilize data obtained in the most recent configuration of the apparatus as well as data taken before the MHS was added.

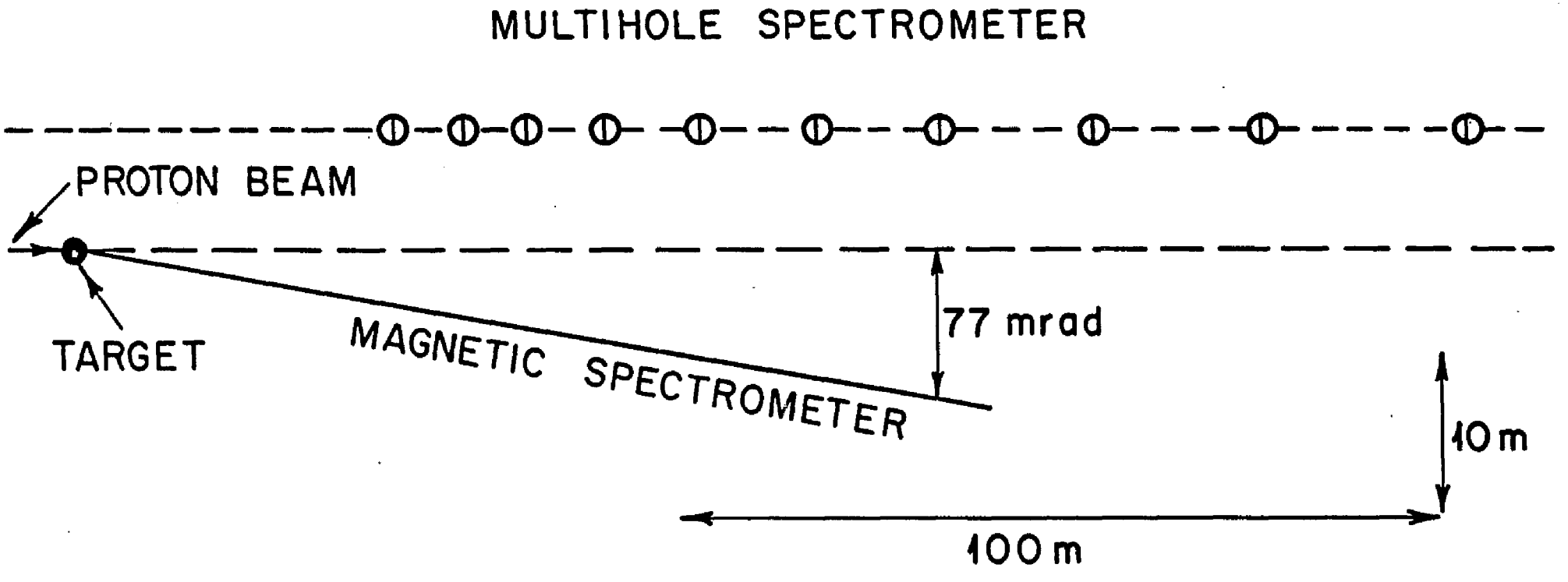
MULTIHOLE SPECTROMETER
PROTON BEAM
TARGET
MAGNETIC SPECTROMETER
77 mrad
10 m
100 m

Fig. 2-1

PRETARGET

The main accelerator cycles approximately every four seconds supplying the Proton Area with a pulse of beam averaging one second long. A total of 2×10^{13} protons were accelerated in the main ring each cycle. The experiment accepted between 10^{12} to 10^{13} protons per pulse on target. The main accelerator and external beam lines are pictured in figure 2-2. The proton beam is slowly extracted at point A, split at points B and C, and finally guided through the pretarget area (figure 2-3) and focused on the target. The beam line and magnetic arm of the spectrometer were all located in tunnels approximately 12 feet below ground level. The beam was focused and positioned on the target through use of a quadrupole magnet doublet (Q1, Q2) and a pair of dipole magnets (D1, D2), to a 1mm diameter circle on the target. The position of the beam was controlled to approximately .5mm, this being especially important in the electron measurement. A secondary emission monitor (SEM) was used to monitor the incident beam intensity. For purposes of absolute normalization the SEM was calibrated periodically by irradiation of gold foils in the incident beam line. The calibration was reproducible to approximately ±5% and the absolute calibration is estimated to have a precision of ±20%.

The incident proton beam possessed a radiofrequency(r.f.) structure acquired upon acceleration; resulting in a bunched beam with buckets of 2 nsec. width and spaced 18.9 nsec. apart. Early in

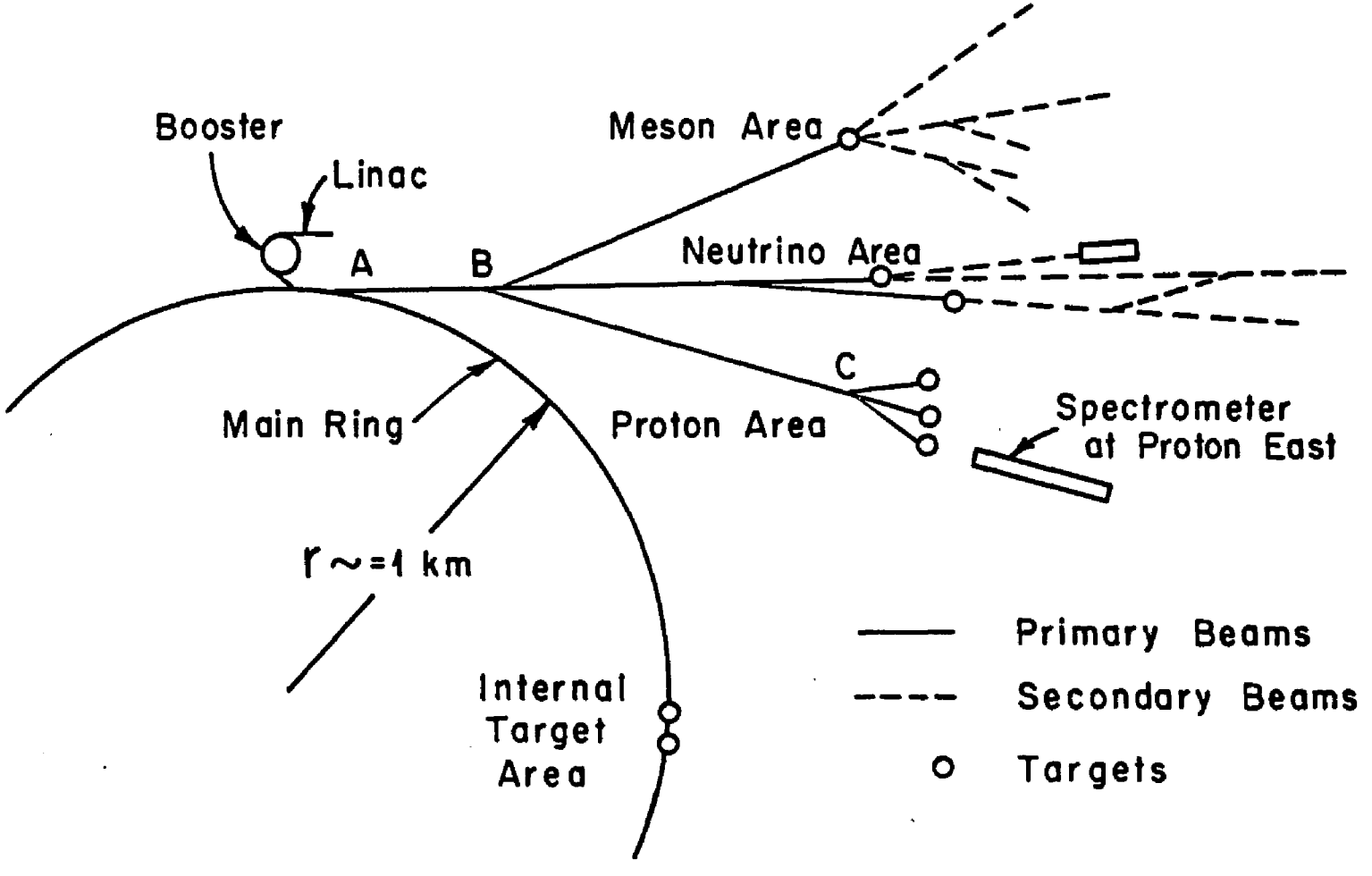

Accelerator and Beam Lines at Fermi National Accelerator Laboratory

FIG. 2-2

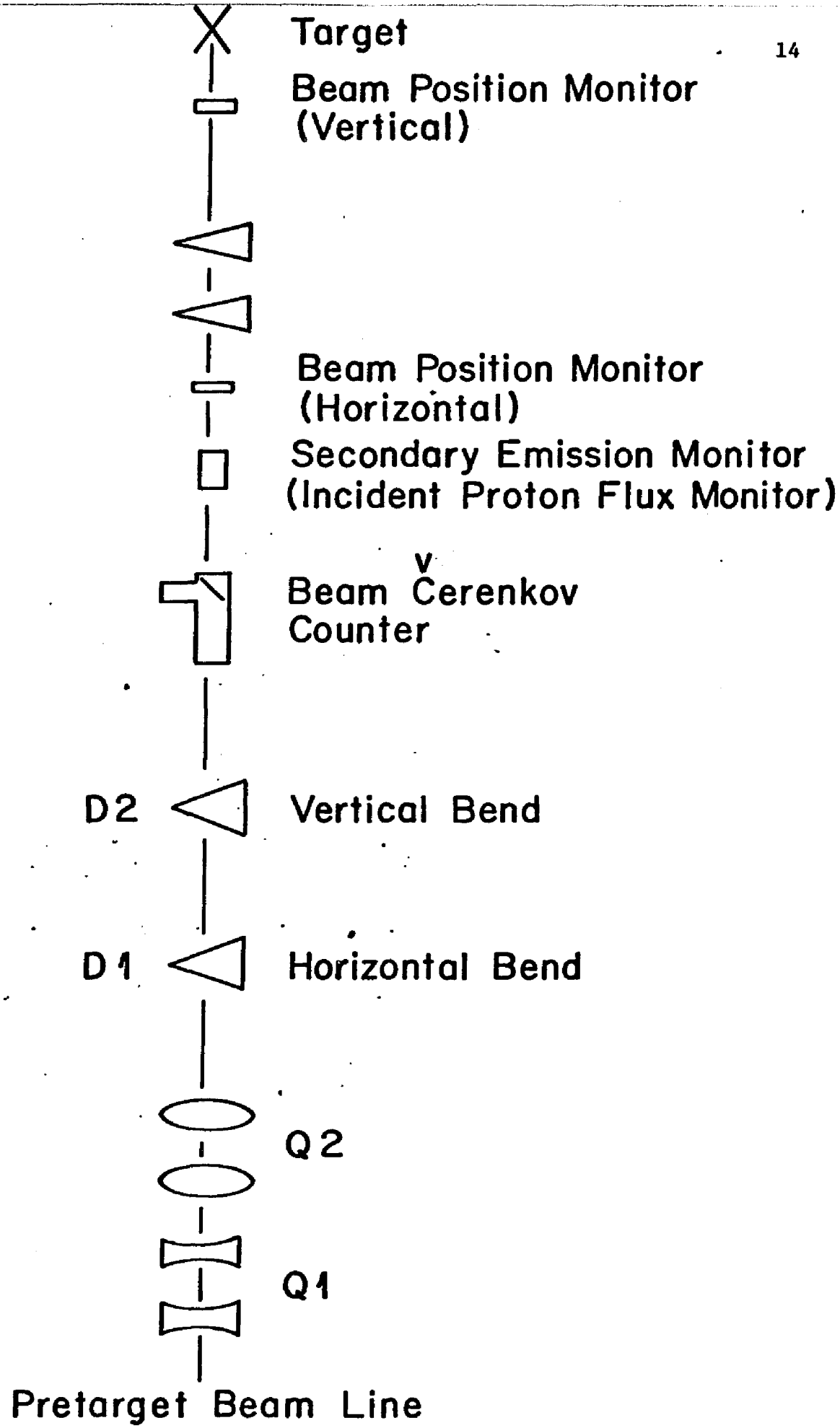
Target
Beam Position Monitor
(Vertical)
Beam Position Monitor
(Horizontal)
Secondary Emission Monitor
(Incident Proton Flux Monitor)
Beam Čerenkov
Counter
D2
Vertical Bend
D1
Horizontal Bend
Q2
Q1
Pretarget Beam Line

FIG. 2-3

the experiment it was determined that the population of these buckets could become extremely uneven and at times the number of protons in a single bucket would be many times the average, which gave rise to what is referred to as "superbuckets". These superbuckets in turn would contribute to an apparent signal in the two arms due to accidental coincidences. For this reason a simple air Cerenkov counter was installed in the incident beam line to measure the number of protons not only in the bucket which triggered the spectrometer, but also in the three buckets prior to and four buckets after the triggering bucket.

The spectrometer was triggered by a requirement in the magnetic arm. The time of any signals originating from the MHS counters within a gate extending from -70 nsec. to +250 nsec. with respect to the trigger signal was then recorded.

Data were taken with three different targets; Beryllium, Tungsten, Copper. All were approximately .4 interaction lengths long. Stacked vertically on a remotely controlled stage, the particular target in use and its vertical position with respect to the beam could be easily changed. The relative luminosity was monitored with two scintillation telescopes at 90° to the incident beam direction. In order to position the beam on the target properly, we scanned the target vertically and horizontally with the beam and observed the ratio of the 90 degrees monitor rate to the rate in the SEM (incident

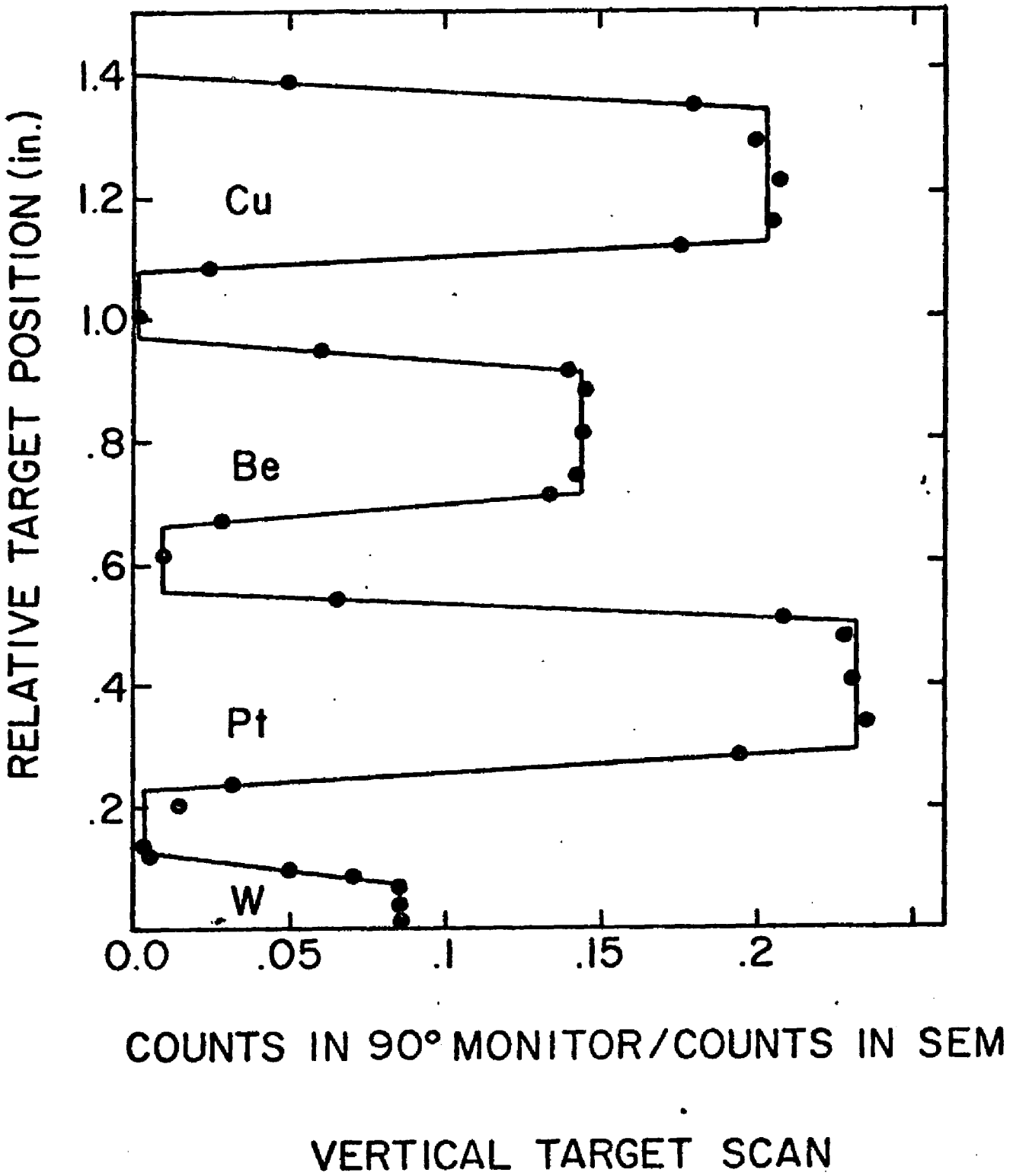
RELATIVE TARGET POSITION (in.)
1.4
1.2
1.0
.8
.6
.4
.2
Cu
Be
Pt
W
0.0
.05
.1
.15
.2
COUNTS IN 90° MONITOR/COUNTS IN SEM
VERTICAL TARGET SCAN

FIG. 2-4

flux). Shown in figure 2-4 is a typical vertical target scan.

SPECTROMETER MAGNETIC ARM

Figure 2-5 shows a schematic view of the magnetic arm of the spectrometer used to detect particles at 77mrad. with respect to the incident beam. The spectrometer possessed vertical and horizontal apertures of ±3.0 mrad. and ±1.5 mrad respectively, approximately defined by the opening of the first quadrupole. The quadrupoles focused particles from the target onto the last hodoscope, 333 feet downstream with a horizontal magnification of approximately 2X and a vertical magnification of approximately 20X. The momentum analysis of the particles was made via two 16mrad. deflections of the central beam. The momentum acceptance of $dp/p = \pm 4\%$ yielded a total acceptance for the magnetic arm of $d\Omega\, dp/p = 1.7 \times 10^{-6}$ ster.. The angular acceptance as a function of momentum is plotted in figure 2-6. The large flux of incident protons, required to investigate production at higher P_T, rendered it impossible to place any counters upstream of the first bending magnet and its associated shielding wall.

The first three trigger counters, A1, A2, A3, were 1/4 inch thick scintillator, 4" wide and 2" high, and A4 6" wide and 3" high. The trigger for all runs except those with an electron trigger consisted of A2, A3, and A4 in coincidence. A1 was not included because of the possibility of inefficiencies due to extremely high singles rates in the upstream end of the detector.

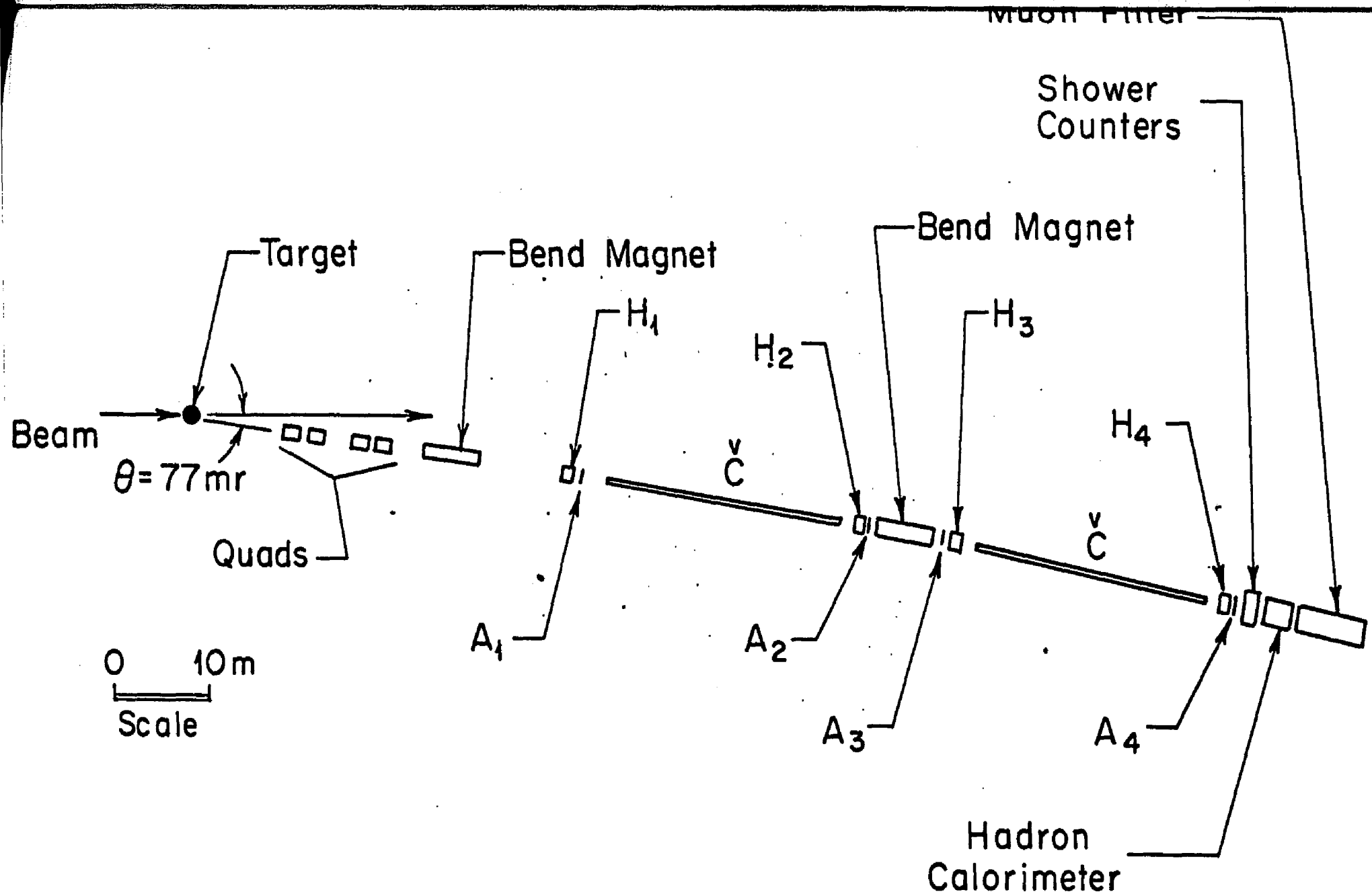

Magnetic Arm of Spectrometer

Fig. 2.5

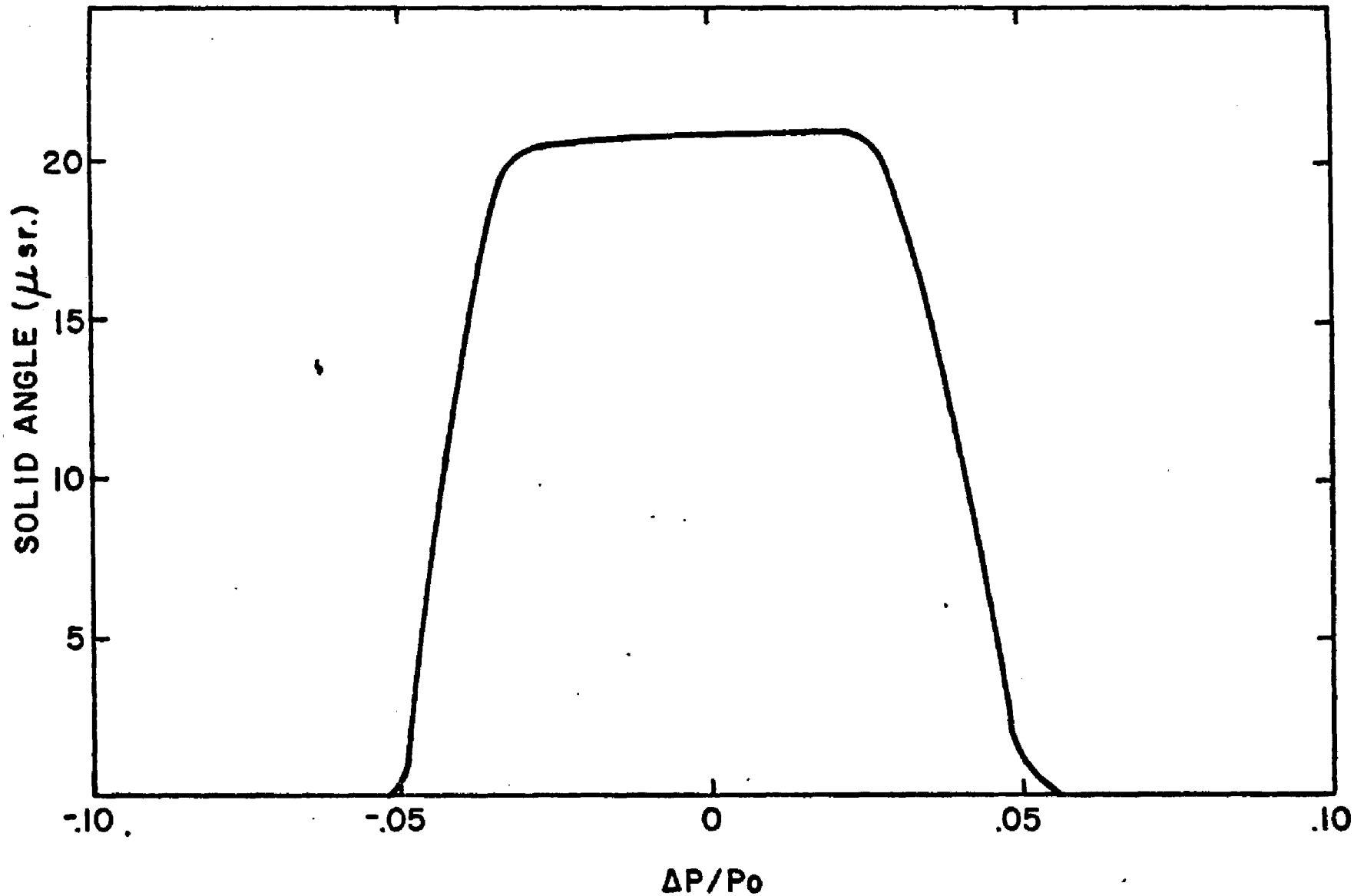

SOLID ANGLE OF MAGNETIC ARM AS A FUNCTION OF ΔP/P, WHERE Po IS THE CENTRAL MOMENTUM AND ΔP IS THE DEVIATION FROM THE CENTRAL MOMENTUM.

FIG.2-6

Track reconstruction was essential when operating the spectrometer at higher momenta in order to eliminate accidental triggers. This was accomplished through the use of the four hodoscopes, labeled H1 - H4. Each hodoscope was composed of three horizontal and nine vertical scintillator elements arranged in an overlapping fashion (figure 2-7) to yield five horizontal and seventeen vertical detection channels. H1, H2 and H3 were equipped with .35" wide horizontal channels and .22" wide vertical channels and H4 with slightly larger horizontal and vertical channels measuring .6" and .35" respectively. This translated into a reconstructed momentum resolution of ±1% and an uncertainty in the reconstructed vertical and horizontal positions at the target of ±.08" and ±.4" respectively. The main advantages gained in employing scintillation hodoscopes as opposed to wire chambers were two-fold: 1) an ability to run at rates approaching 10 MHz in A1 2) the ease in maintaining trouble free performance of the hodoscopes.

The identification of particles triggering the spectrometer was accomplished in part by two Cerenkov counters (C1, C2), one placed between the H1 and H2, and the other between H3 and H4. Each counter consisted of an 80 foot long, 1 foot diameter stainless steel tube on one end of which was bolted a 6 foot long tube containing the optics. A schematic drawing of the optics is shown in figure 2-8. Cerenkov light emitted at angles less than 9mrad. was collected in one two-inch photomultiplier tube (RCA 3100M); light emitted between 9mrad and 38mrad. was directed to a second photomultiplier. A

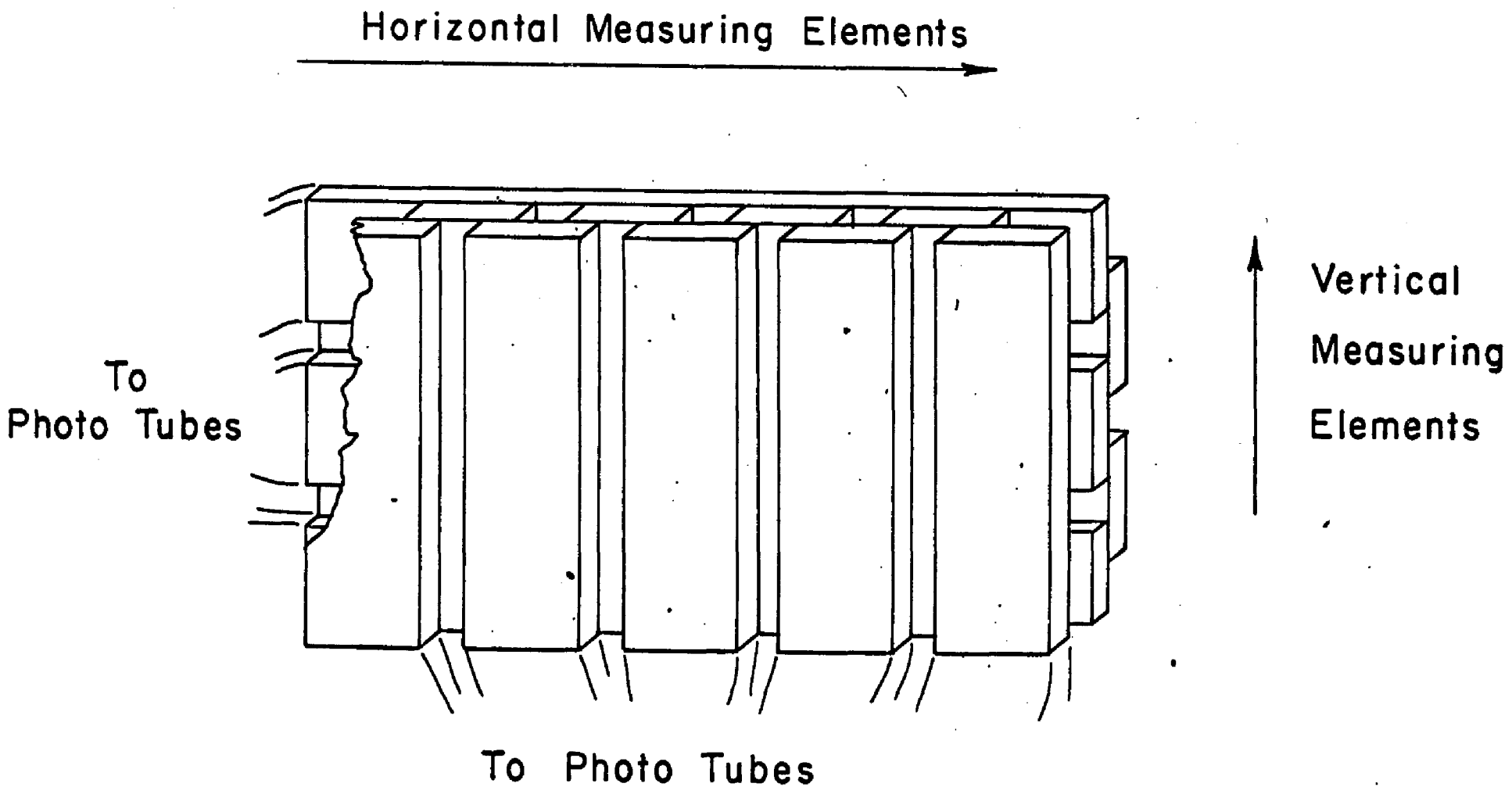

Hodoscope Layout

FIG. 2-7

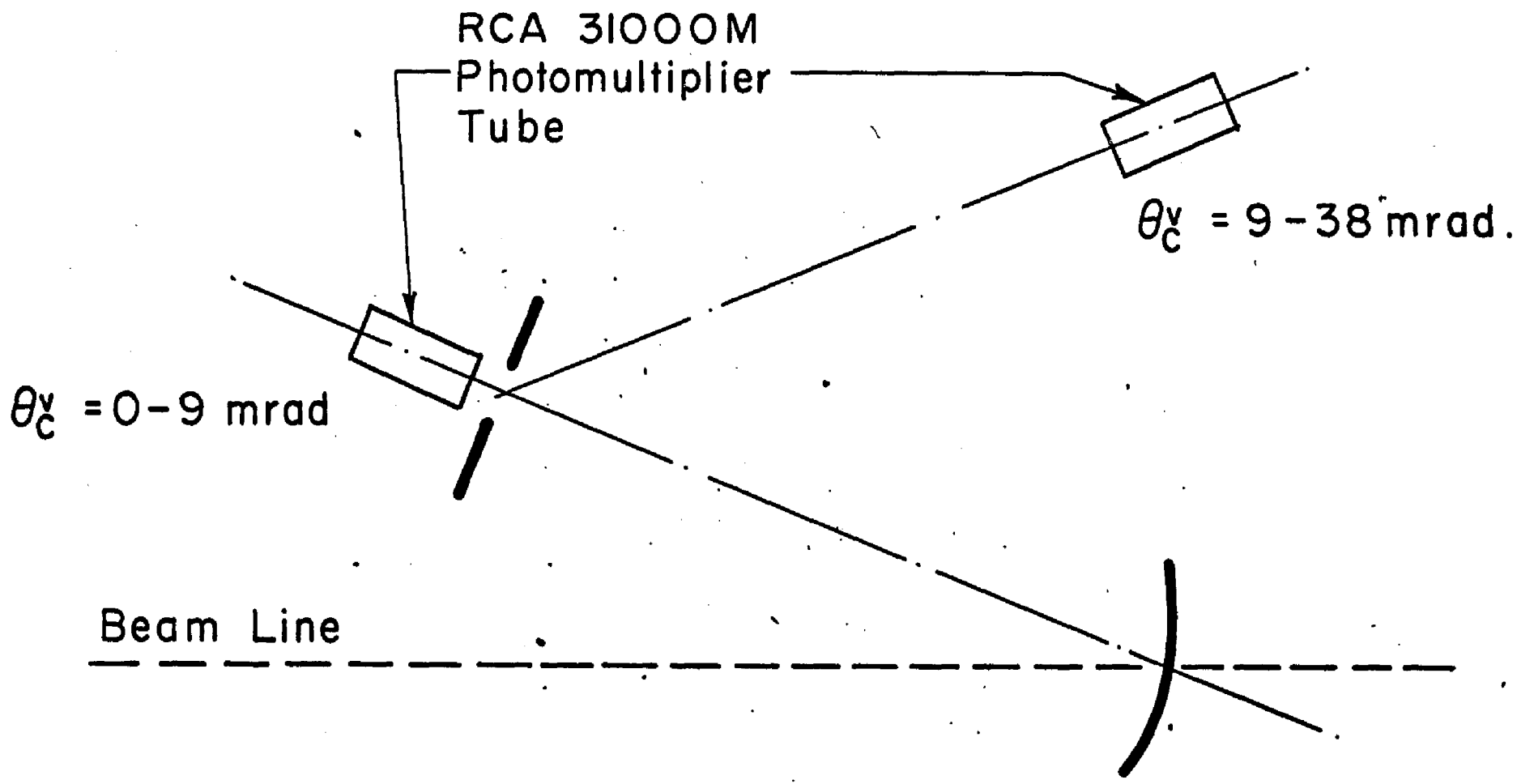

Schematic View of $\check{C}$erenkov Optics

Fig. 2-8

typical mode of operation entailed adjusting the pressure and gas type in C1 and C2 to count in the following way:

	0-9 MRAD.	0-38 MRAD.
C1	K	π μ e
C2	π μ e	-----

As such, the protons and kaons would possess unique signatures and pions, muons and electrons identified as a group needing to be further distinguished.

The gas pressure in each counter could be varied from .1 to 10 atmospheres and was continuously measured to a precision of ±.1%. The entire counter was kept in thermal equilibrium with a water jacket through which a continuous flow of water was maintained. The temperature was monitored at five positions along the length of the tube and determined to be constant within ±.5% C.

PARTICLE IDENTIFIER

A particle identifier was placed at the downstream end of the spectrometer to provide further discrimination between electrons, muons and hadrons. It was divided into three distinct units; an

electron shower counter, a hadron calorimeter, and a muon filter.

The shower counter was composed of four identical modules, the construction of which is detailed in figure 2-9. Eleven layers, alternating between 3/16" thick lead sheets and 1/4" thick sheets of scintillator provided 5.1 radiation lengths of radiator per module. There were 20 radiation lengths in total. The light from each module was guided to a Amperex 58DVP photomulitplier tube and the pulse height measured with an LSR - 2248 analog-digital converter (ADC).

An electron shower could produce a signal corresponding to as many as 500 minimum ionizing particles. The photomultiplier used would saturate under these conditions. For this reason the light was attenuated by placing a black paper mask over the face of each photomultiplier, transmitting only 3% of the scintillation light. Shower energies could be measured with an accuracy of 10% but minimum ionizing particles were below threshhold.

The shower counter was primarily employed to discriminate between electrons and pions. A detailed discussion of its use and effectiveness are deferred to Chapter Three.

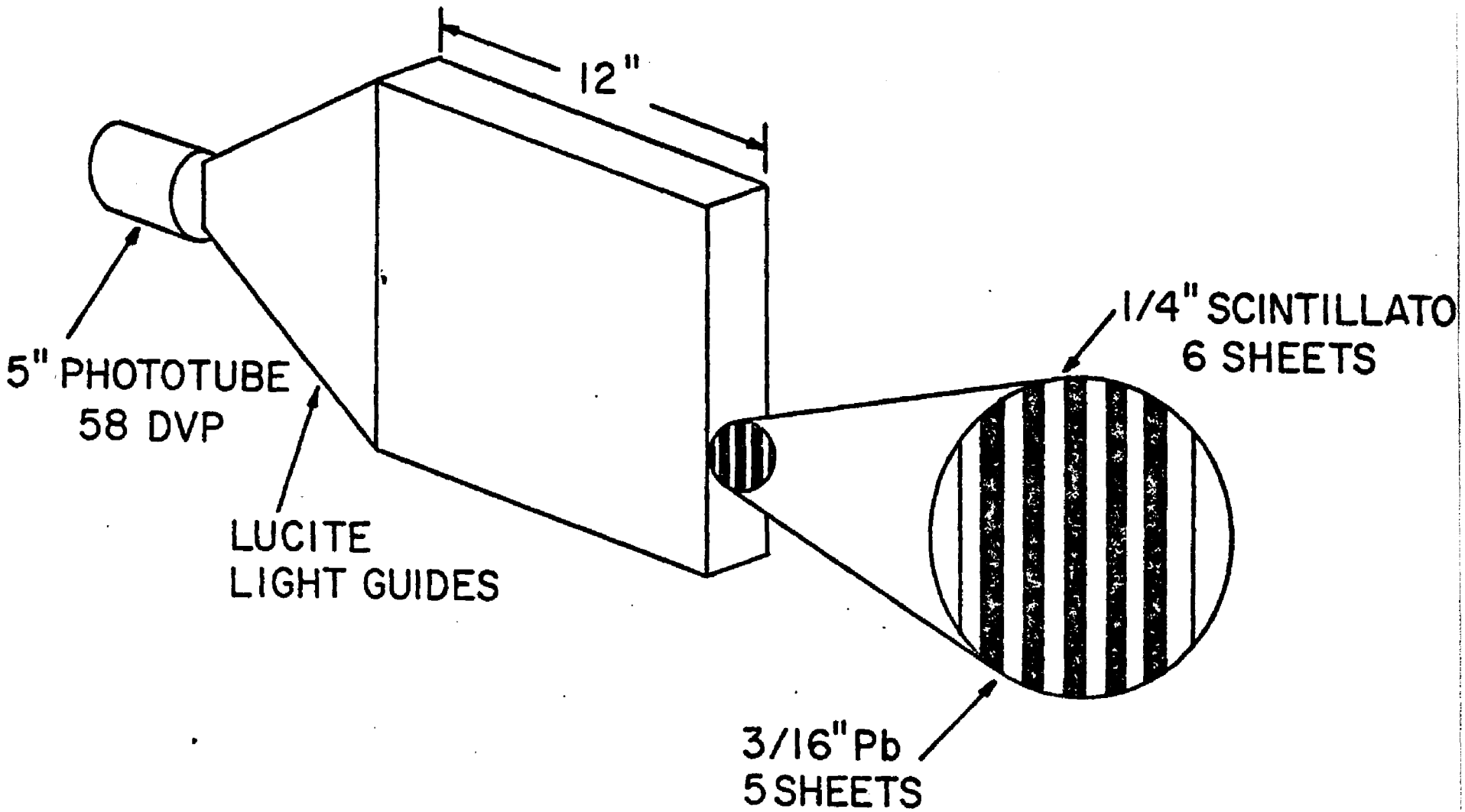

SHOWER COUNTER MODULE

FIG. 2-9

The hadron calorimeter was located directly behind the shower counter. It consisted of 10 identical modules. Each module was composed of a 6" x 12" x 12" block of iron with a 12" x 12" sheet of scintillator placed against the downstream end of the block. Each scintillator was attached to a RCA 6655 photomultiplier tube. The integrated pulse heights for all tubes were recorded for each event trigger. The total length of the calorimeter was approximately 6 feet, corresponding to 8.7 absorption lengths.

The last element in the magnetic arm was the muon filter. Its construction differed from the hadron calorimeter only in the amount of iron and the sampling distance. There was a total of 12' of iron in the muon filter. A scintillation counter was placed after every 2' block of iron.

In order to measure muon yields from nontrival sources it was essential to attenuate the hadron flux in the spectrometer beam line, and hence the decay muons from pions and kaons. This was accomplished by placing two movable absorbers between the target and the spectrometer(figure 2-10). The first absorber consisted of a tungsten block, 23" long, inserted into the beam line with its upstream end 9.5" from the target center. A 42" iron block was used as a second absorber, with its upstream end 42" from the target center. Alternating the insertion of each absorber allowed extrapolation of the muon signal to zero decay path length. In addition, with an absorber in place the spectrometer could operate with an incident

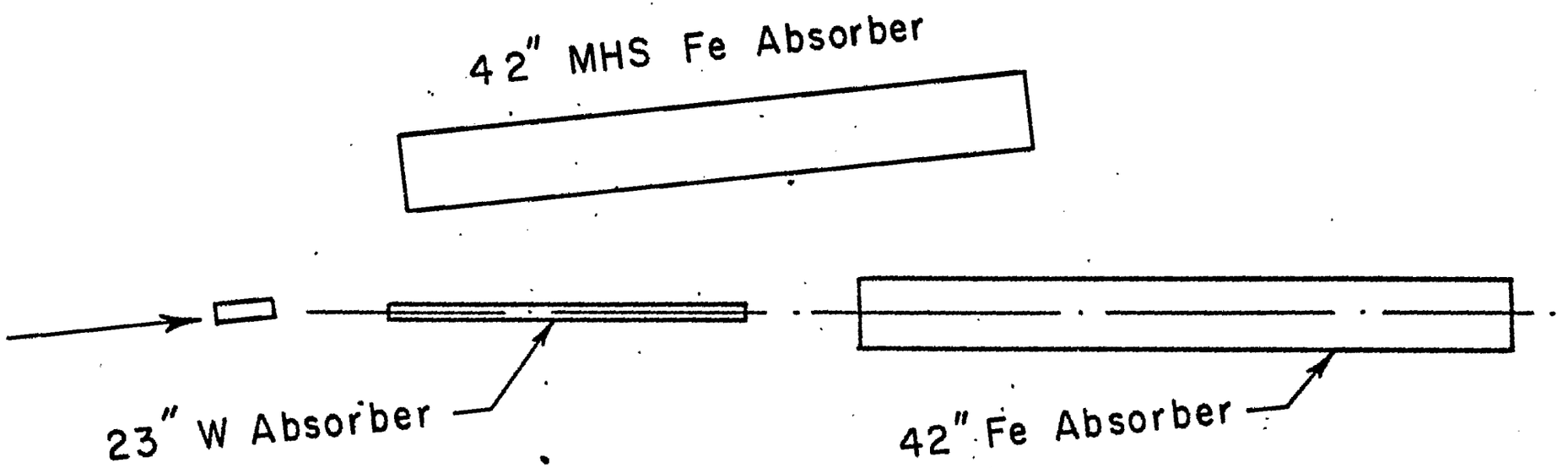

Absorber Configuration in Target Box
All Absorbers Are Movable

Fig. 2-10

proton flux 100 times greater than without it.

MULTI HOLE ARM

The multihole spectometer arm was installed to look for muons in coincidence with a particle triggering the magnetic arm. It consisted of ten 3.6 x 1.1 x .1 m^3 tanks of liquid scintillator placed in holes in the ground. Each tank was equipped with an Amperex 58DVP photomultiplier tube viewing each end. The holes lay in a line nearly parallel to, and displaced appproximately 20' from, the primary beam line (see figure 2-1).

The soil and iron shielding located between the multi-holes and the target provided a natural hadron absorber, and allowed only muons with P_T >3.2 GeV to reach the hole detectors. Figure 2-11 shows the detector efficiency as a function of transverse momentum for a muon emitted at the target into the solid angle subtended by the MHS. This function was calculated with a monte carlo simulation of the muon energy loss in the material between the target and the MHS.

In the laboratory system the MHS was efficient over a range of -8° Φ 25° in the azimuth and 2.25° θ 7.73° in the polar angle. The polar angle subtended by the MHS in the proton-nucleon center of mass was 60° θ 126° (figure 2-12)

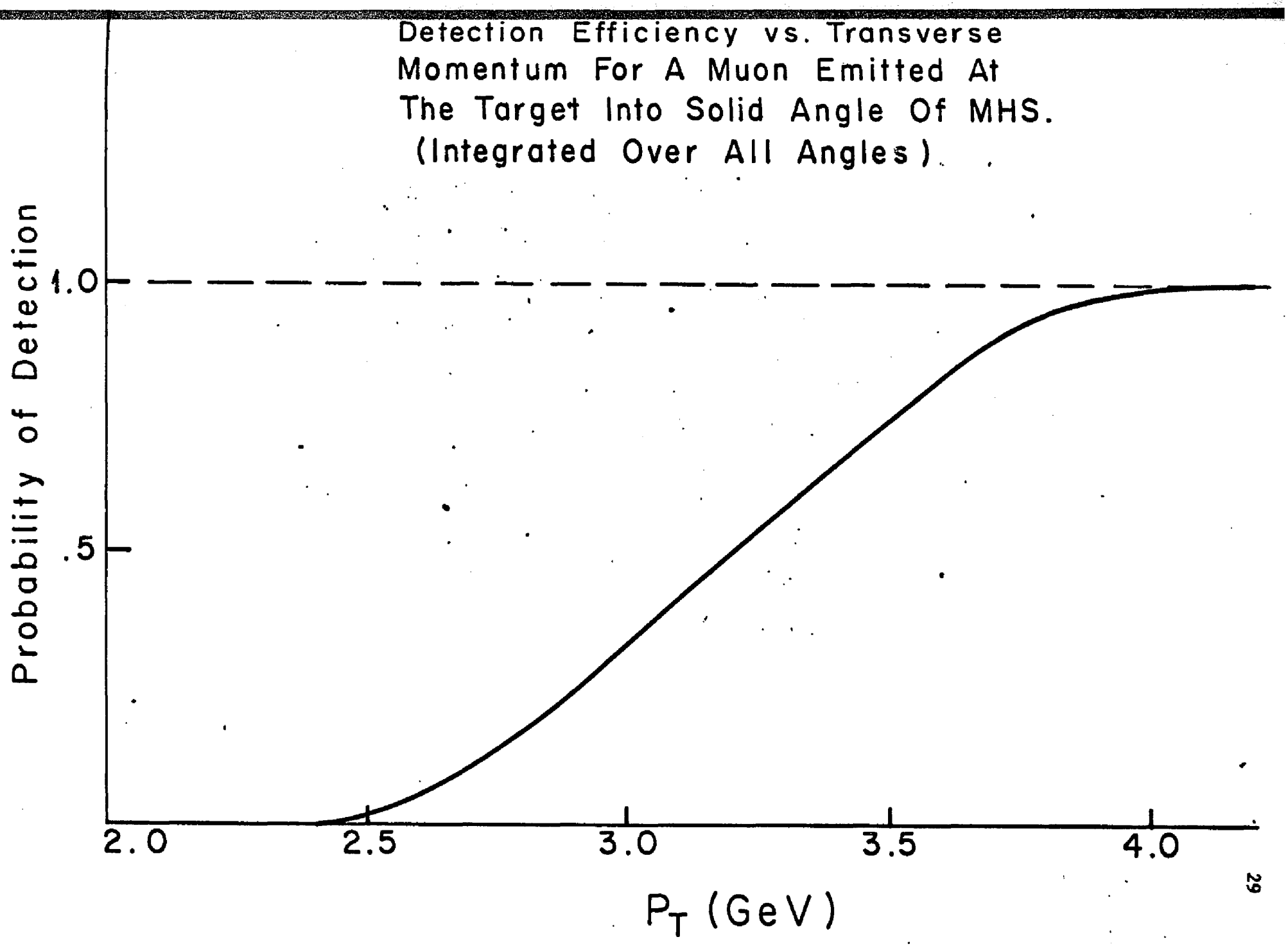
Detection Efficiency vs. Transverse
Momentum For A Muon Emitted At
The Target Into Solid Angle Of MHS.
(Integrated Over All Angles)
Probability of Detection
1.0
.5
2.0
2.5
3.0
3.5
4.0
P_T (GeV)

FIG. 2-11

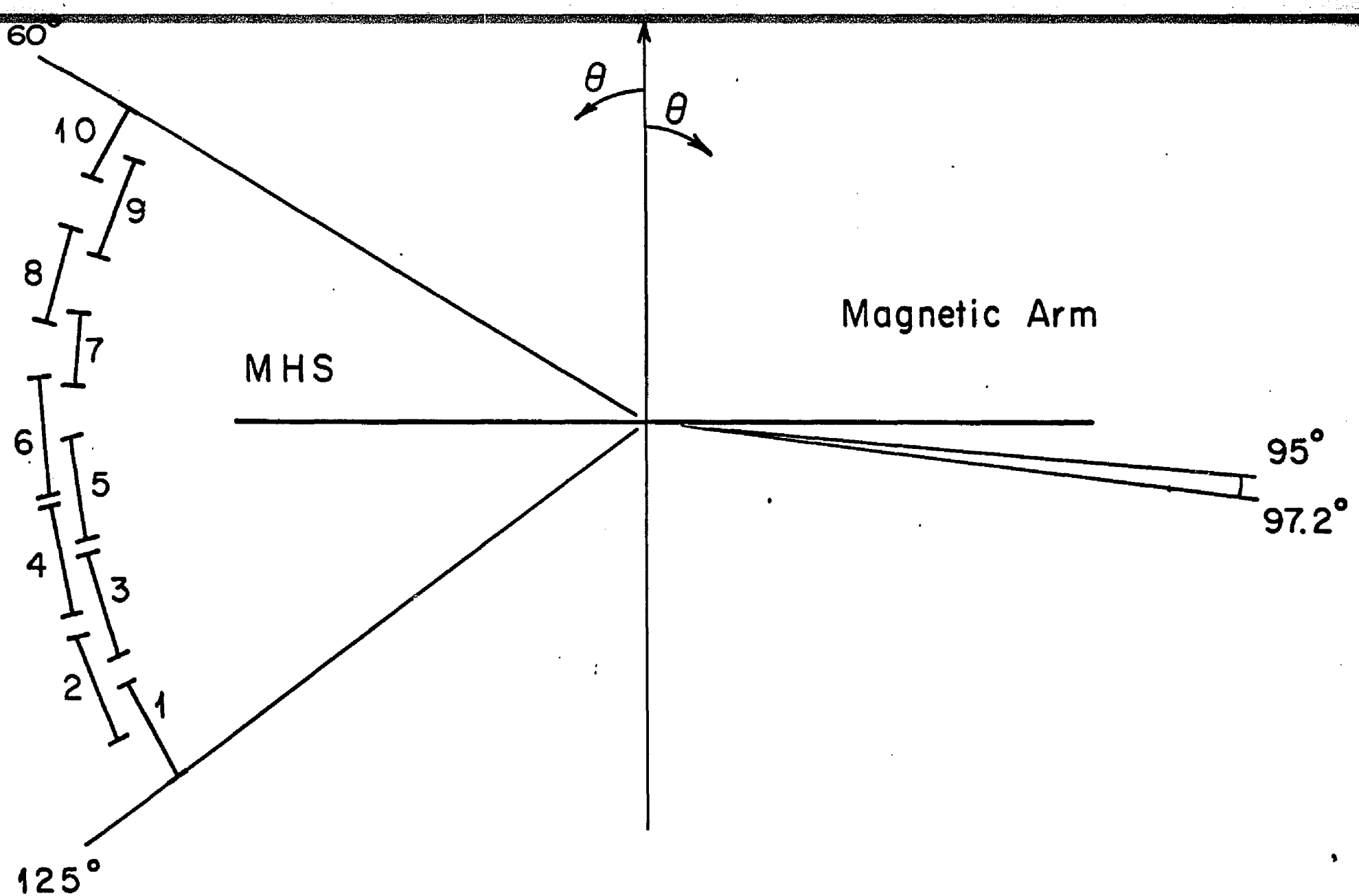

Polar Angle Subtended In The pN Collision
CM Frame (In The Beam-Spectrometer Plane)
400 GeV Beam

FIG. 2-12

DATA ACQUISITION

A set of data recorded during January 1977 has been analyzed as a test of scaling in muon pair production. The conclusions are reported elsewhere[17]. For this report the same set of data are analyzed together with previous data to present a compilation of results dealing with direct single muon production by proton-nucleus collisions. Data were taken on Beryllium, Tungsten, Copper targets for various configurations of incident proton momentum, spectrometer momentum, and polarity.

In addition, a short run was made with a trigger that increased the fraction of events containing an electron in the spectrometer. The aim was to search for high mass electron-muon pairs at 60 GeV spectrometer momentum with 400 GeV protons incident on an 8" Be target. Data were collected using the spectrometer in three mutually exclusive modes: (1) hadron (2) muon (3) electron. Exactly what constituted each data type and why it was taken is explained below.

When measuring hadron yields the spectrometer was run with absorbers removed and an A2*A3*A4 coincidence trigger. The pion yields in particular provide a very convenient normalization for the lepton measurements. The lepton yields are more reliably expressed in terms of ratios with respect to pions because of the poor absolute

normalization available, although, in most cases the limited statistics determined the uncertainty. The hadron (no absorber) runs were also needed to correct the muon yield measurements. They were used to remove the contribution due to hadrons decaying downstream of the absorbers (Chapter 3).

Muon data were collected alternating the insertion of the two absorbers into the secondary beam line (detailed description in Chapter 3). The absorbers functioned as hadron attenuators, in effect shortening the average decay path for the pions and kaons. Two absorber lengths were used to allow extrapolation to zero decay path length.

Special runs enhancing the fraction of electrons in the trigger were necessary to avoid the dead time that would have been involved in recording every pion event along with the electron events. The trigger employed was

$$T = A2 * A3 * A4 * (CA1 + CA2)$$

where A2 * A3 * A4 was the usual trigger. CA1 and CA2 represent signals from each of the Cerenkov counters.

For electron runs the Cerenkov counters were operated in the threshold mode. The pressures in the Cerenkov counters were adjusted so that pions with momenta $P = 1.05\ P_{spectrometer}$ were below

threshold. With this constraint the electrons produced a signal in both Cerenkov counters of 3.5 photoelectrons, on the average yielding a detection efficiency of 97%. A Cerenkov pulse height spectrum for a sample of electrons is shown in figure 2-13. The one and two photoelectron peaks are clearly visible.

Converted photons from pi-zero decay provide a large contribution to the observed yield. In order to estimate this contribution the amount of converter present in the secondary beam line was varied. This was accomplished by changing the transverse position of the beam on the target. Data were collected with average exit path lengths through the target of 3.83 mm., 12.57 mm., and 37.10 mm.

A length of 3.83 mm. corresponded to a configuration where only half the beam was incident on the target. Since we were rate limited by the spectrometer and not by the incident proton flux available, the incident beam was directed such that it partially missed the target and proportionally increased in intensity. This increased the direct component of the observed signal without reducing the data collection rate. The flux incident on the target was monitored by observing the ratio of the 90° monitor to the SEM.

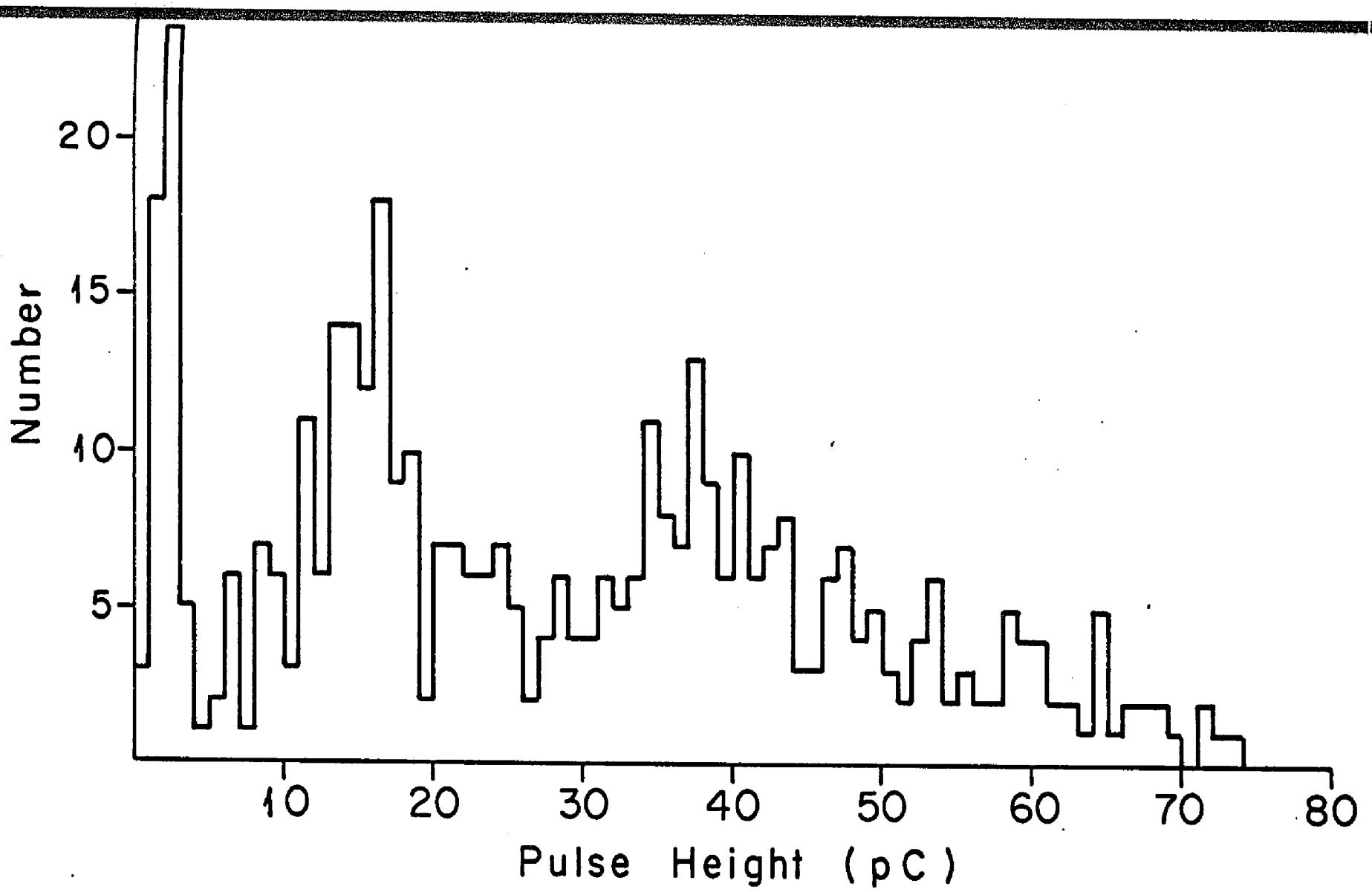

Histogram of Pulse Height From A Single Cerenkov Counter For A Sample of Electrons

FIG. 2-13

Following each trigger the analog and timing information from all counters was collected by a Camac data acquisition system. An online PDP - 9 computer read the data from the Camac system. At the end of each pulse of beam, the event records along with all scalers and monitoring information (eg. pressures, temperatures) were written on magnetic tape.

CHAPTER 3

DATA REDUCTION

In this chapter we first describe the analysis procedures applied to the data to extract the raw particle yields. Following this, we discuss the corrections used to obtain the final particle ratios and cross-sections. The data are analyzed on a pulse by pulse basis. All events which occurred during a specific pulse of incident beam are either rejected or retained for further analysis subject to the following criterion:

1) The beam is well centered on the target. Evidence of this is provided by requiring that the ratio (number of particles traversing the 90 degree montor) / (number of particles traversing the SEM) remains constant(within 5%).

2) The incident beam intensity as a function of time contains no gross structure (spikes) throughout the beam spill. This insures against any significant change in the instantaneous rate and hence, changes in the efficiency of the counters in the spectrometer.

In addition to the examination of data on a pulse by pulse basis, more subtle indicators of problems were checked for each run. For example, a small deviation of the incident beam off vertical center resulted in loss of acceptance because of the large vertical magnification of the spectrometer. Runs with vertical asymmetries in the rear hodoscope were rejected.

TRACK RECONSTRUCTION

After a particular pulse of beam is determined to be acceptable, each individual event is unpacked from the tape record and undergoes a series of tests to determine whether its track coordinates are consistent with a single particle traversing the spectrometer. Accidental events were eliminated in this round of analysis. To describe the reconstruction procedure we defined a coordinate system. The z-axis was defined by the trajectory which passes through the horizontal and vertical center of the spectrometer elements (bending magnets, quadropoles, etc.). A particle which follows this trajectory is said to have a momentum equal to the central momentum, p_{spec} , of the spectrometer. The x and y axes were defined as the horizontal and vertical rays perpendicular to the z-axis.

Referring to figure 3-1, the x and y coordinates of the particle track at H1-H4 were first assumed to be given by the center of the struck hodoscope element. If more than one hit exists in a hodoscope, analysis of the event was terminated. The steps in reconstructing the event are given below:

TRACK RECONSTRUCTION IN THE BENDING PLANE OF THE SPECTROMETER.

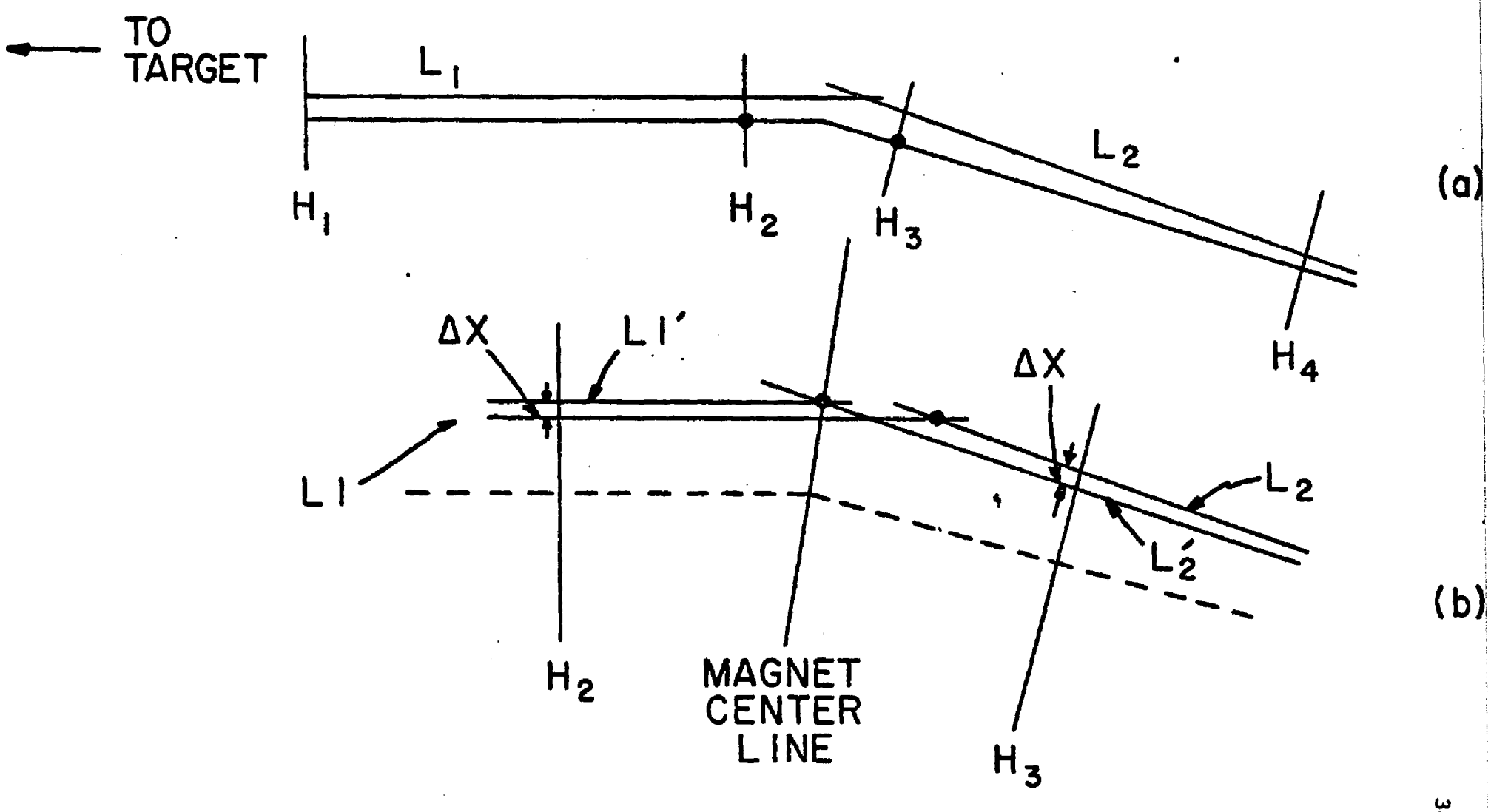

FIG. 3-1

1. The coordinates in H1 and H2 define line L1, and the coordinates in H3 and H4 define line L2.

2. The coordinates in H2 and H3 are then moved in equal amounts($\Delta X, \Delta Y$) to find lines L1' and L2' which meet in the center of the second bending magnet, BM2.

3. At this stage the data are required to satisfy the following requirements(see figure 3-2)

   1. $\Delta x < .25"$

   2. $\Delta y < .35"$

   3. $dy/dz_{L1} - dy/dz_{L2} < .001$

4. The angle of bend in BM2 is calculated for L1' and L2' and then used to extrapolate from H1 through BM1 and back to the target. (x_t, y_t)

5. Lastly, we require the reconstructed interaction position (x_t, y_t) to be consistent with being located inside the target.

This procedure eliminated the major component of accidental triggers which ranged from 3% to 5% of the total event sample depending on the

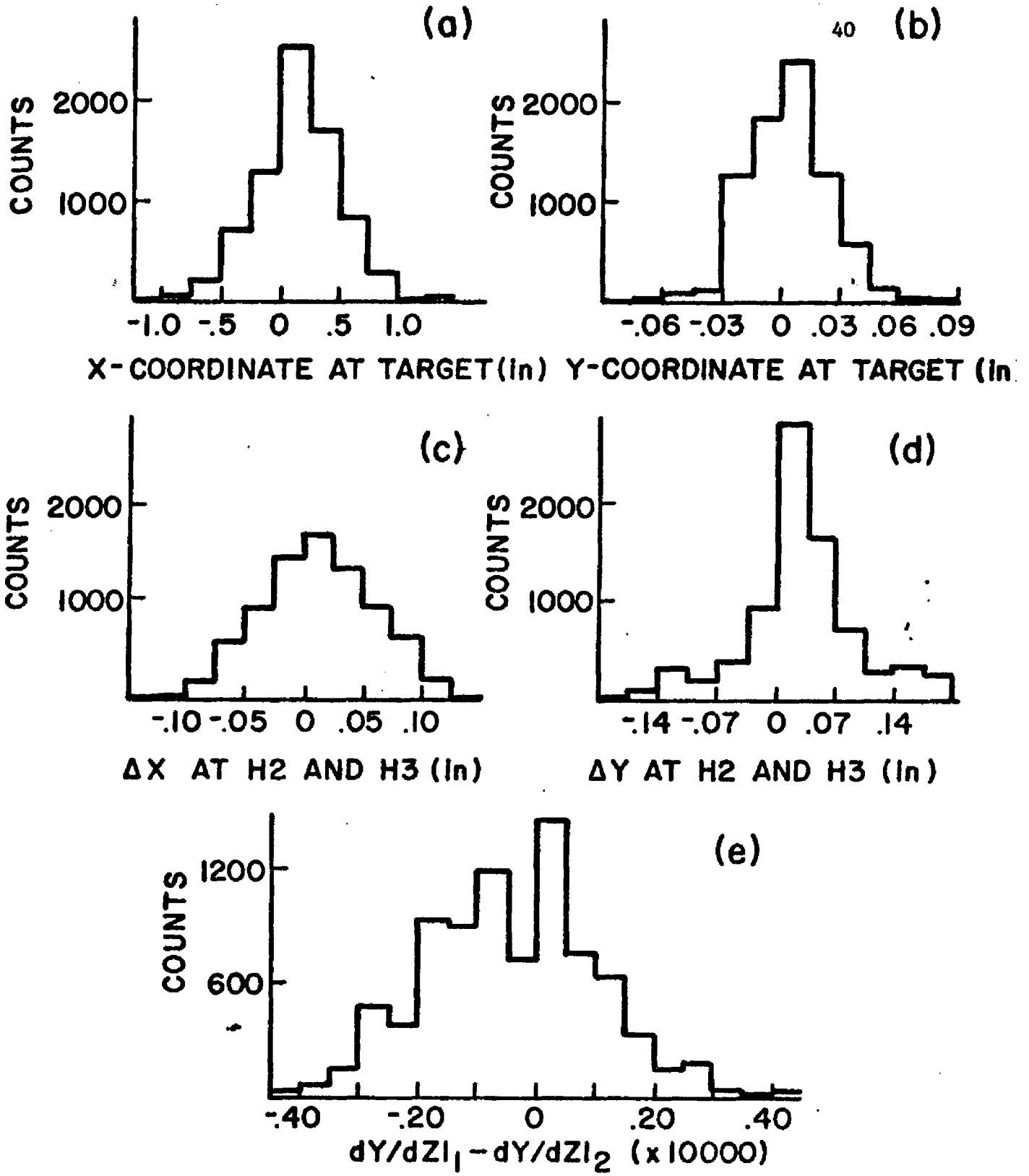

DISTRIBUTION OF RECONSTRUCTION PARAMETERS
(a) X-POSITION AT TARGET, (b) Y-POSITION AT TARGET,
(c) ERROR IN MEASURED X-POSITION AT H2 AND H3,
(d) ERROR IN MEASURED Y-POSITION AT H2 AND H3,
(e) CONTINUITY IN SECOND BENDING MAGNET

FIG. 3-2

momentum setting of the spectrometer. The accidentals consisted mainly of a random hit in A2 in coincidence with a muon passing thru A3 and A4.

PARTICLE IDENTIFICATION

The Cerenkov counter, as described in Chapter 2, was used to identify the particles traversing the spectrometer; they belong to one of three groups: (1) π, μ, e (2) K (3) P. In each running mode of the spectrometer, the separation of pions from the lepton signal was the most formidable problem. The trigger for both the muon and electron measurements discriminated against hadrons by factors of approximately 150 and 250 respectively. The additional discrimination was supplied by making use of the particle identifier.

Muons were identified with 17 feet of iron interspersed with scintillation counters in the hadron calorimeter and muon filter. Events characterized by pulse heights in 5 out of the 6 muon counters(M1-M6) above the pedestal were defined to be muons. This requirement was essentially 100% efficient for identifying muons passing through the spectrometer. For example, all events in which M1 through M3 were hit were found to have hits in counters M4 through M6.

The separation of the pion and muon signal by the muon filter was corroborated by the hadron calorimeter. Shown in figure 3-3 is the separation induced by the muon filter as viewed via the "energy deposition" in the calorimeter. Any additional discrimination through

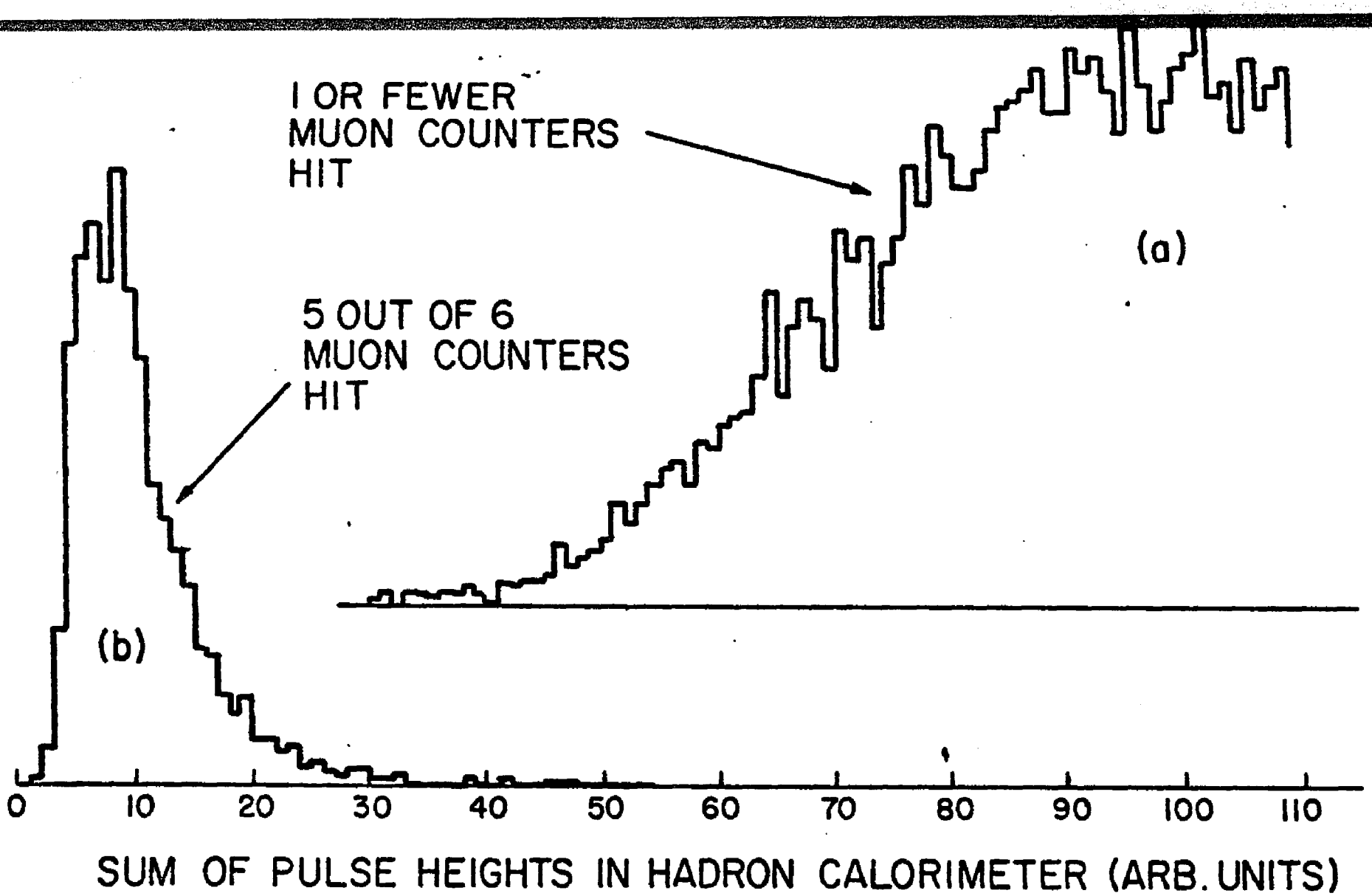

ENERGY DEPOSITION IN CALORIMETER FOR PARTICLES DEFINED AS (a) HADRONS, (b) MUONS.

FIG. 3-3

use of the hadron calorimeter was not helpful. Pions that decayed in the spectrometer were the only significant contamination to the direct muon signal. In comparison, contamination of the muon sample due to pion punch through or other mechanisms was negligible.

Electron identification was accomplished through use of the shower counter in conjunction with the hadron calorimeter. The discrimination against pions by the Cerenkov trigger alone allows the electron signal to be seen in the raw data over a background of pions. Figure 3-4(a) displays a histogram of the energy deposited in the shower counter for all events which passed the geometrical cuts (i.e. found to originate in the target). The visible electron peak in the raw data assures us that the electron signal is not induced by the restrictions applied to the data.

Three characteristics of a shower were used to distinguish an electron from a pion:

(1) Total energy deposited in the shower counter

(2) Shower shape

(3) Penetration depth into detector

In order to make these cuts without loss of electron detection efficiency, a test group of "pure" electrons was obtained by requiring at least two photoelectrons in each Cerenkov counter. Figure 3-5 displays the response of the various counters to this sample along with the cuts chosen. The shower shape was selected by requiring the pulse heights in counters E1 through E3 to be above the values shown,

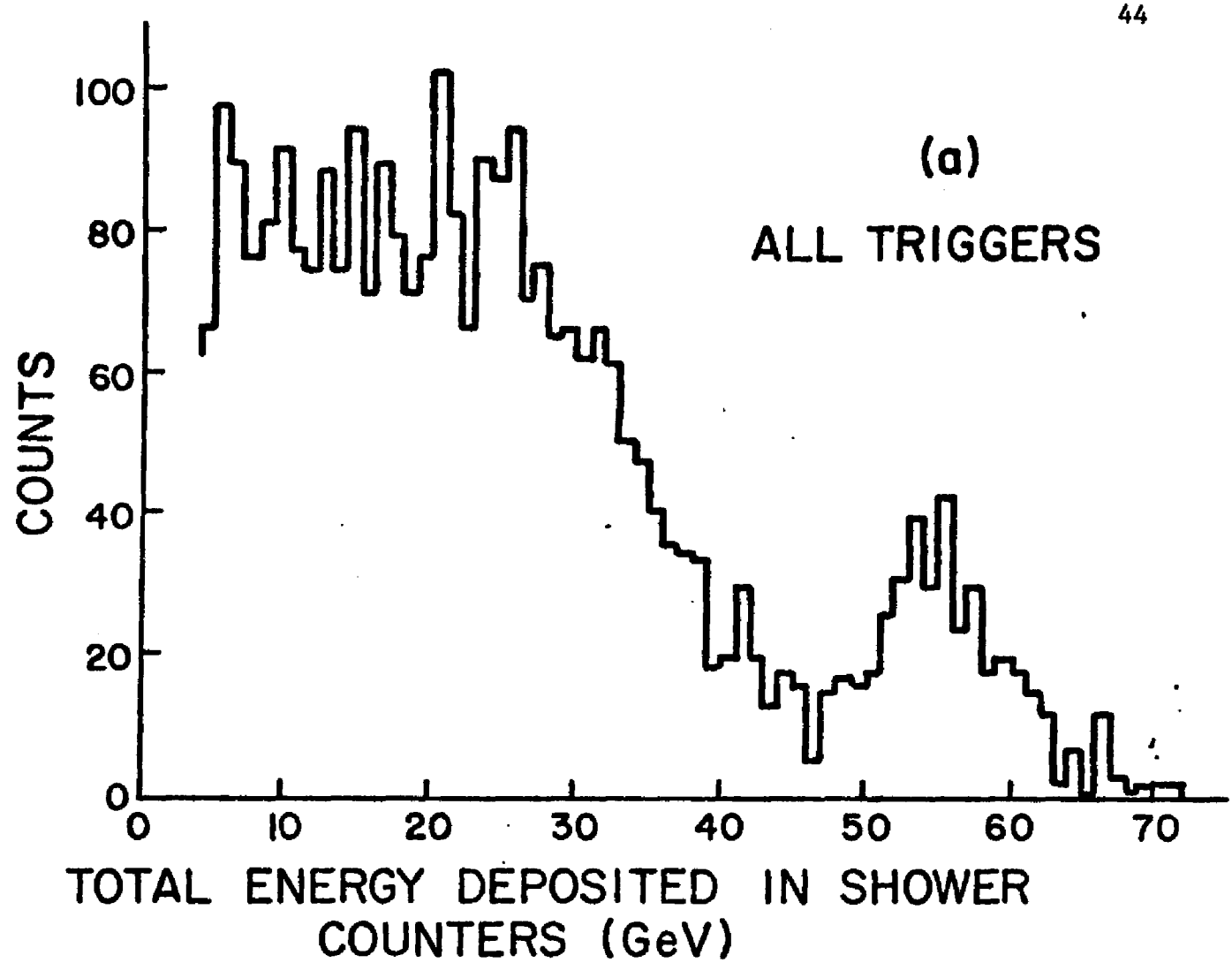
(a)
ALL TRIGGERS
COUNTS
100
80
60
40
20
0
0
10
20
30
40
50
60
70
TOTAL ENERGY DEPOSITED IN SHOWER COUNTERS (GeV)

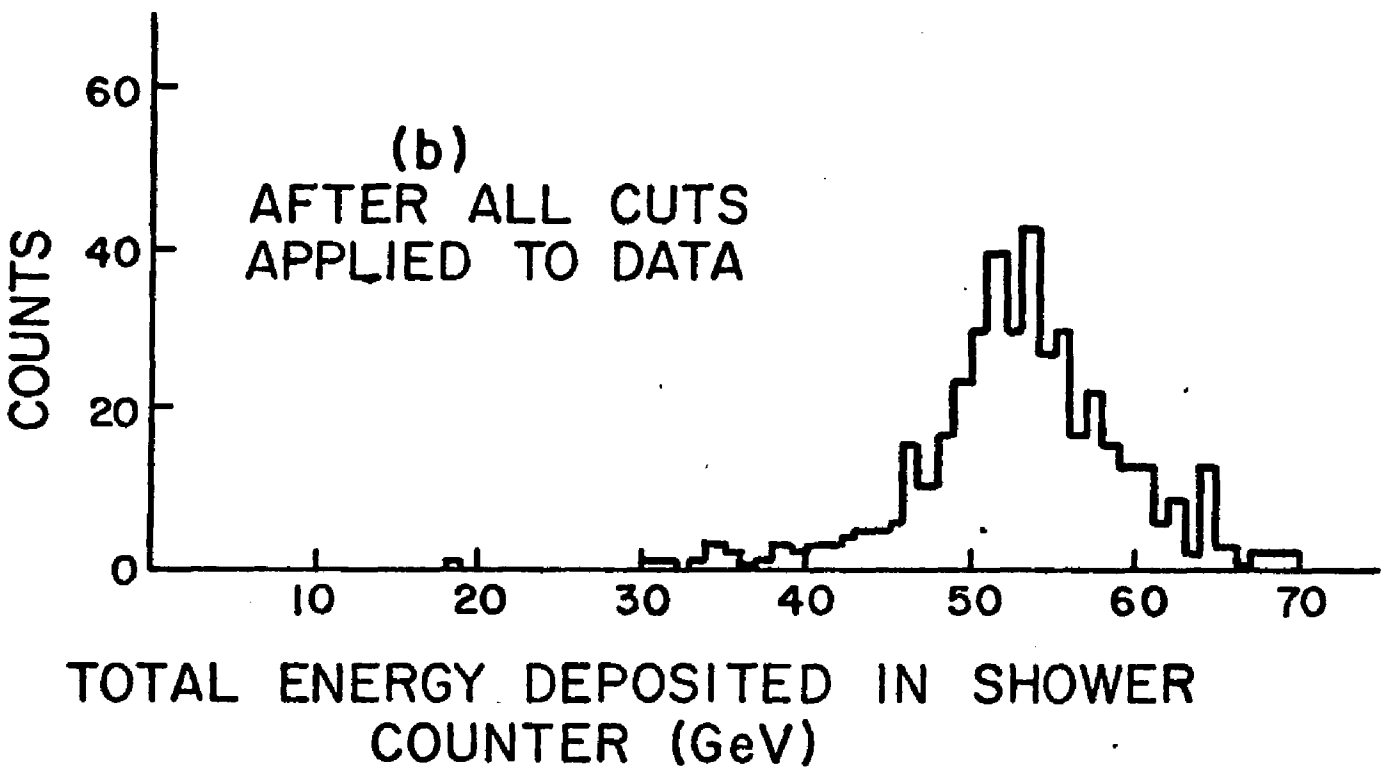
(b)
AFTER ALL CUTS APPLIED TO DATA
COUNTS
60
40
20
0
10
20
30
40
50
60
70
TOTAL ENERGY DEPOSITED IN SHOWER COUNTER (GeV)

FIG. 3-4

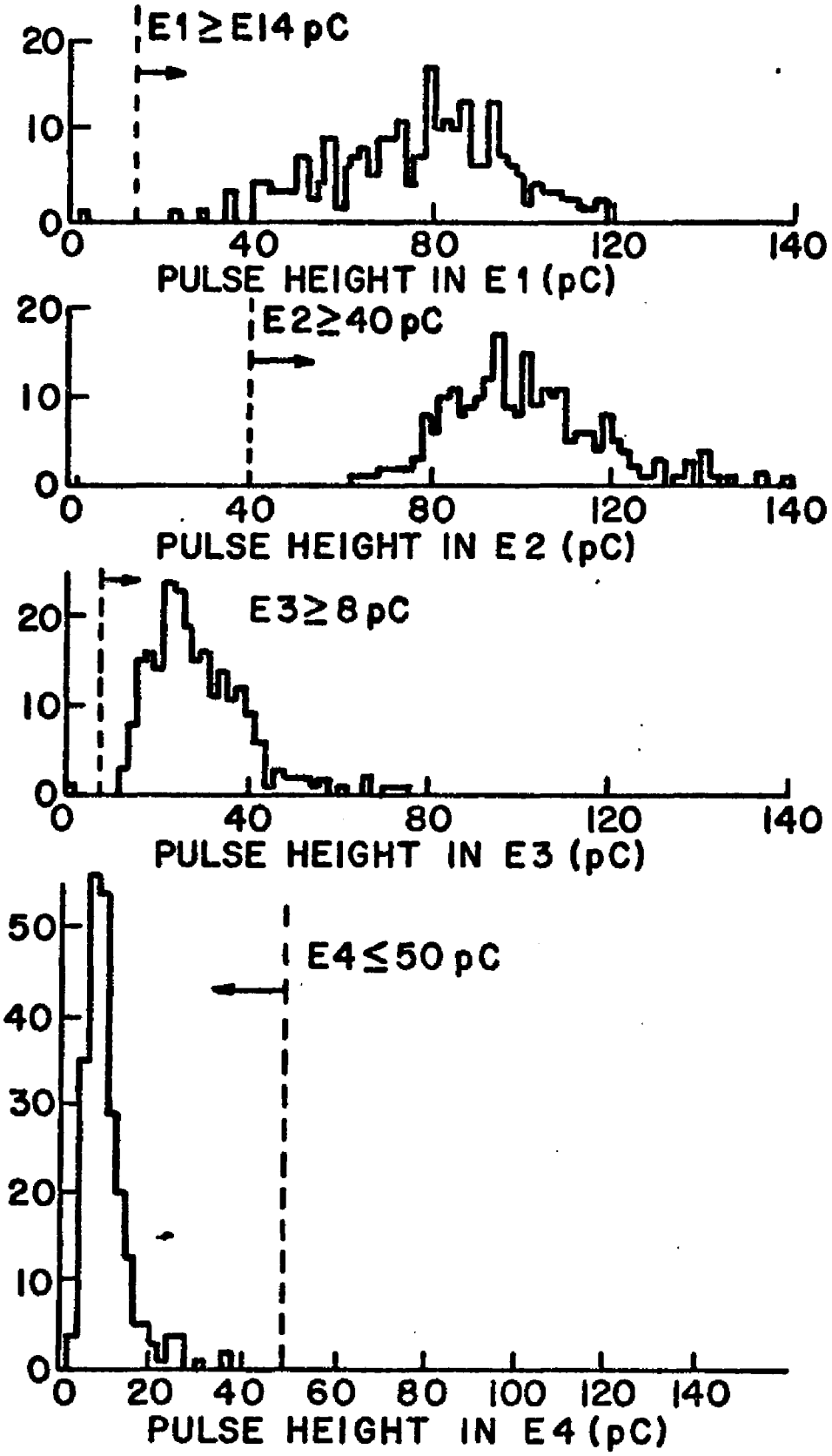

PULSE HEIGHT DISTRIBUTIONS IN SUCCESIVE SHOWER MODULES (E1-E4) FOR A SAMPLE OF ELECTRONS. FROM THESE DISTRIBUTIONS THE CUTS SHOWN ABOVE WERE USED TO DISTINGUISH ELECTRONS FROM HADRONS.

FIG. 3-5

and E4 to be below the upper bound given. Requirements on the length of the shower were controlled by an upper limit on the pulse height in counter F1. Applying all these to the "normal" data sample resulted in the total shower energy distribution shown in figure 3-4(b.)

The contribution of misidentified pions to the electron signal was calculated by analyzing data for which the absorber was inserted into the spectrometer beam line. In this sample we were able to measure the fraction of pions incident on the shower counter that were misidentified as electrons because all real electrons stopped in the absorber. The fraction of pions misidentified as electrons was:

$$f_{e-pi} = 4.3 \times 10^{-3}$$

The resulting hadron contamination in the lepton yields after the above cuts were applied to the data were:

(1) Pion contribution to observed muon yield 3×10^{-5} μ/π

(2) Pion contribution to observed electron yield 7×10^{-5} e/π

MULTI-HOLE ANALYSIS

Events which survive reconstruction and identification in the magnetic arm were then subjected to analysis of the multi-hole counters. All hole counters possessed two photomultipliers at each end of the tank(see page 26). Each was connected to a TDC (time digitizer). The TDC measures the time of flight of the incident muon with respect to the trigger. If both TDC'S associated with a single tank were stopped in the event, a muon was assumed to have traversed the counter.

Two quantities were then formed from the corrected TDC'S:

Σ = time of flight = (TDC 1 + TDC 2) / 2

Δ = vertical position in tank = (TDC 2 - TDC 1) / 2

This averaged time of flight to the tank eliminated the dependence on the photon transit time inside the tank. The time of flight to Multi-hole 1 is histogrammed in figure 3-6(a.) for a pion triggering the magnetic arm.

No analysis is done in terms of this time of flight. Instead, all events in each of the individual peaks are assigned to an R.F. bucket. So in terms of the analysis we see figure 3-6(a.) as pictured in 3-6(b.). Here bucket number 4 is the R.F. bucket in time

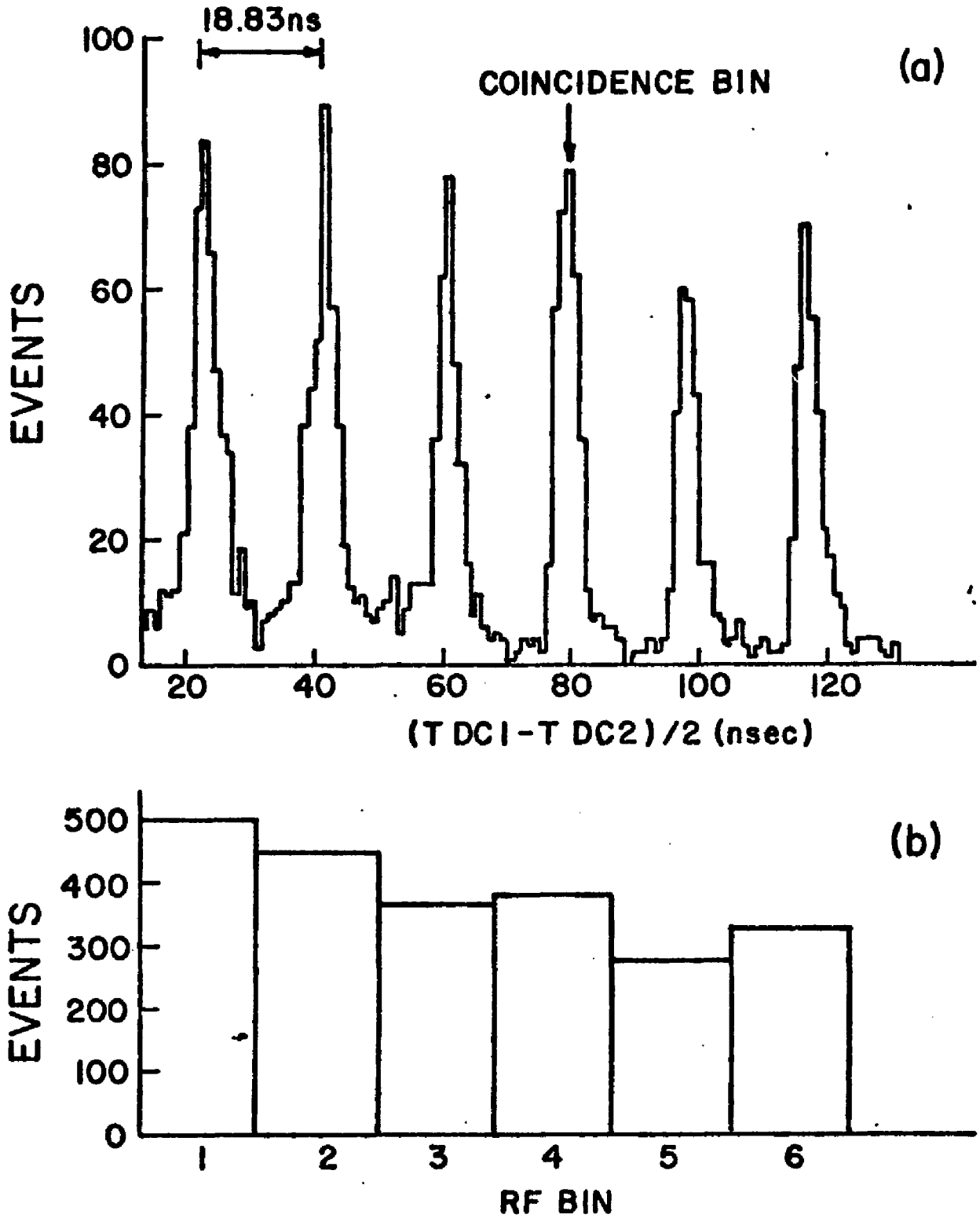

MHS 1 SIGNAL TIME DISTRIBUTION RELATIVE TO PION TRIGGER IN MAGNETIC ARM.

FIG. 3-6

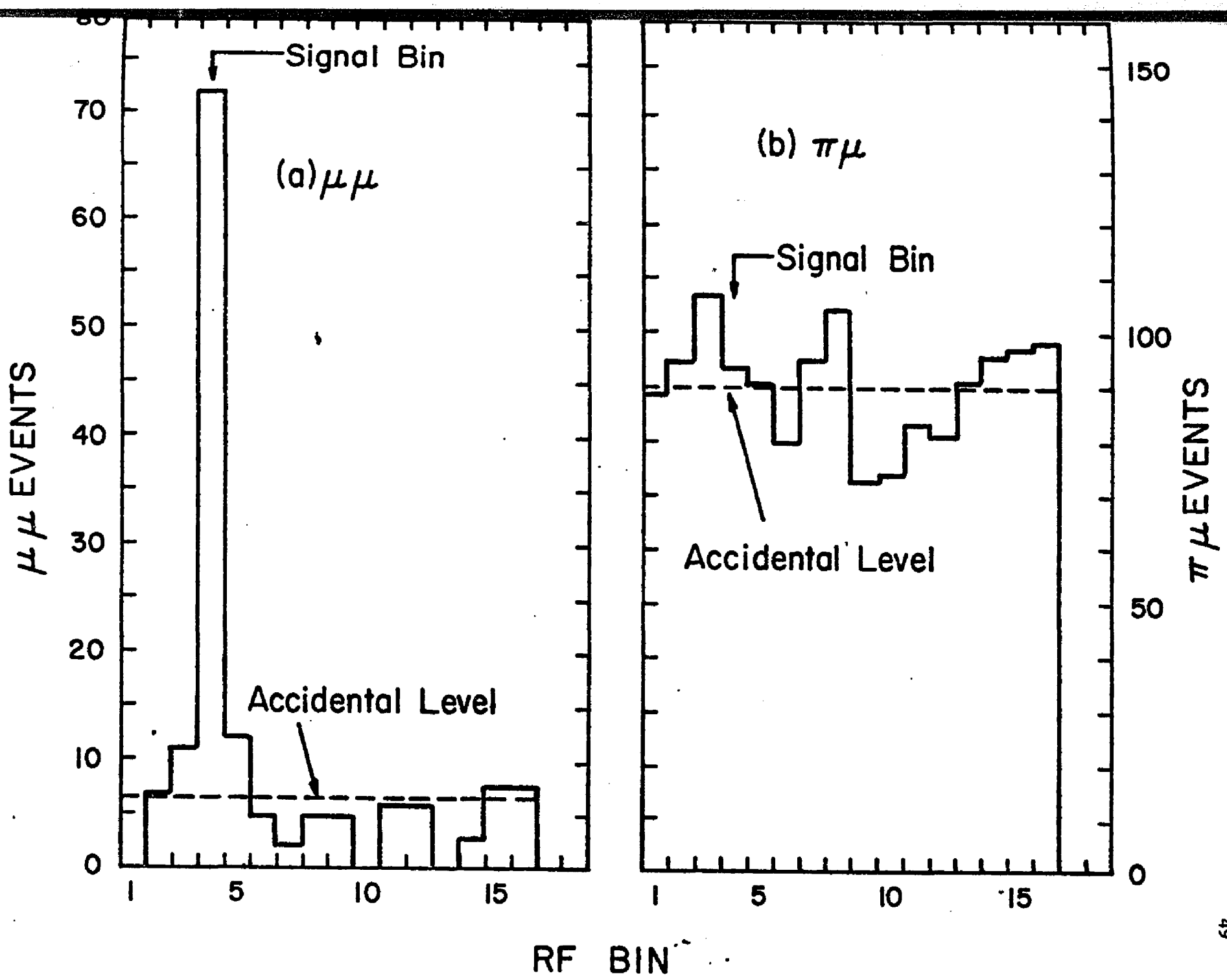
Signal Bin
(a) μμ
Accidental Level
μμ EVENTS
0
10
20
30
40
50
60
70
1
5
10
15
(b) πμ
Signal Bin
Accidental Level
πμ EVENTS
0
50
100
150
1
5
10
15
RF BIN

FIG. 3-7

with the trigger in the magnetic arm. The other buckets measure the accidental coincidences between the two arms. Any difference in the in-time bin over the out-of-time bins constitutes a coincidence signal after intensity fluctuations in the incident proton beam are taken into account (see Chapter 2). In figure 3-7 are displayed the raw data for μ-μ and π-μ coincidences. The μ-μ signal is obvious, on the other hand, we find no apparent π-μ coincidences.

CORRECTIONS TO THE DATA

DERIVATION OF CROSS SECTIONS AND particle RATIOS

PIONS

All analysis of leptons was carried out in terms of ratios with respect to pions. For this reason we discuss pions first. The invariant cross section per nucleus for pions as measured by the magnetic arm is given by:

$$E\frac{d^3\sigma}{dp^3} = \frac{A}{\rho L N_o}\,\frac{Y}{p^2\,\Delta\Omega\,(\Delta p/p)}\,F$$

A = atomic number of target nuclei

ρ = density of target

L = length of target

N_o = Avagadro's number

Y = observed yield of pions per incident proton

$d\Omega(dp/p)$ = spectrometer acceptance = 1.7×10^{-6}

p = central momentum acceptance by spectrometer

F = correction factors to the yield of pions = (D)(T)(S)

The correction factor, denoted in the above formula as F, is composed of three parts.

1) Decay Correction - loss of pions due to their decays throughout the spectrometer. This effect ranges from 2.5% at P_{spec} = 80 GeV / c to 9.5% at P_{spec} = 20 GeV / c. The length of the decay path(L_{DEC}) is given by the distance from the target to the front of the particle identifier, 103m.

$$D = e^{L_{DEC}/\gamma c \tau}$$

where $\gamma = E_\pi / m_\pi$

$\tau = \pi^\pm$ LIFETIME AT REST $= 2 \times 10^{-8}$ sec.

2) Absorption in the target - In this factor we correct for the attenuation of the incident proton beam along with the attenuation of the pions produced inside the target This correction factor ranged from 1.06 for the Be target to 1.18 for the Cu target.

$$T = e^{\lambda_{TARG}}$$

where λ_{TARG} = # of absorption lengths traversed in target.

3) Absorption in the spectrometer - In this factor we correct for pion absorption by the material in the secondary beam line. All material, type and amount, located in the secondary beam line is listed in Appendix I. The correction is given by:

$$S = e^{\lambda_s}$$

λ = the number of absorption lengths of material the particle must pass through in the spectrometer

MUON ANALYSIS

Muon data were taken for spectrometer momenta between 20 GeV/c and 80 GeV/c. For each data point three types of runs were necessary for a complete measurement: (1) no absorbers in place (2) the tungsten absorber in place (3) the iron absorber in place.

With one of the absorbers in place the principal sources of muons were:

I) muons from pion and kaon decay downstream of the absorber

II) muons from pion and kaon decay upstream of the absorber

III) "direct" muons

The run with no absorber in place was utilized in two ways. Firstly it was used to derive the pion yields with which we normalize the lepton yields. Secondly, the decay muon contribution from hadrons which punch through the absorber was found by measuring the muon signal with no absorber inserted. In this configuration the number of hadrons and hence the number of muons from source (I.) is increased by a factor of 200. Subtracting source (I.) from the raw muon yield we find the raw muon yield from sources (II.) and (III.)

$$\mu_i^{1,2} = \mu_i^{1,2,3} - (\mu_o/\pi_o)\pi_i$$

The subscript indicates the type of absorber, if any, employed during

the measurement, and the superscript denotes the sources.

To separate sources numbered (II.) and (III.) one needs information about how each type of absorber and its position in the beam line affects the acceptance of the spectrometer. These effects are of three general types:

1) Loss of muons in the secondary beam due to multiple scattering in the absorber.

2) Broadening of the acceptance distribution due to multiple scattering in the absorber.

3) Energy loss of muons upon traversing the spectrometer.

(1) and (2) of above are related and dependent on the location of the absorbers. The tungsten absorber, which was located very near the target will widen the acceptance. Single muon production is a very steep function of transverse momentum. Therefore, muons produced at angles slightly smaller and outside of the acceptance can be scattered into the spectrometer and contribute at a significant level.On the other hand, the iron absorber is located one meter downstream; at this point particles scattered into the spectrometer will have trajectories that do not point back to the target. Generally speaking, the iron absorber can scatter out but cannot scatter in. The tungsten absorber can scatter in as much as out. Figure 3-8 shows a comparison of the acceptances of the Fe and W absorbers for 40 GeV/c muons as compared with the acceptance with no absorbers inserted.

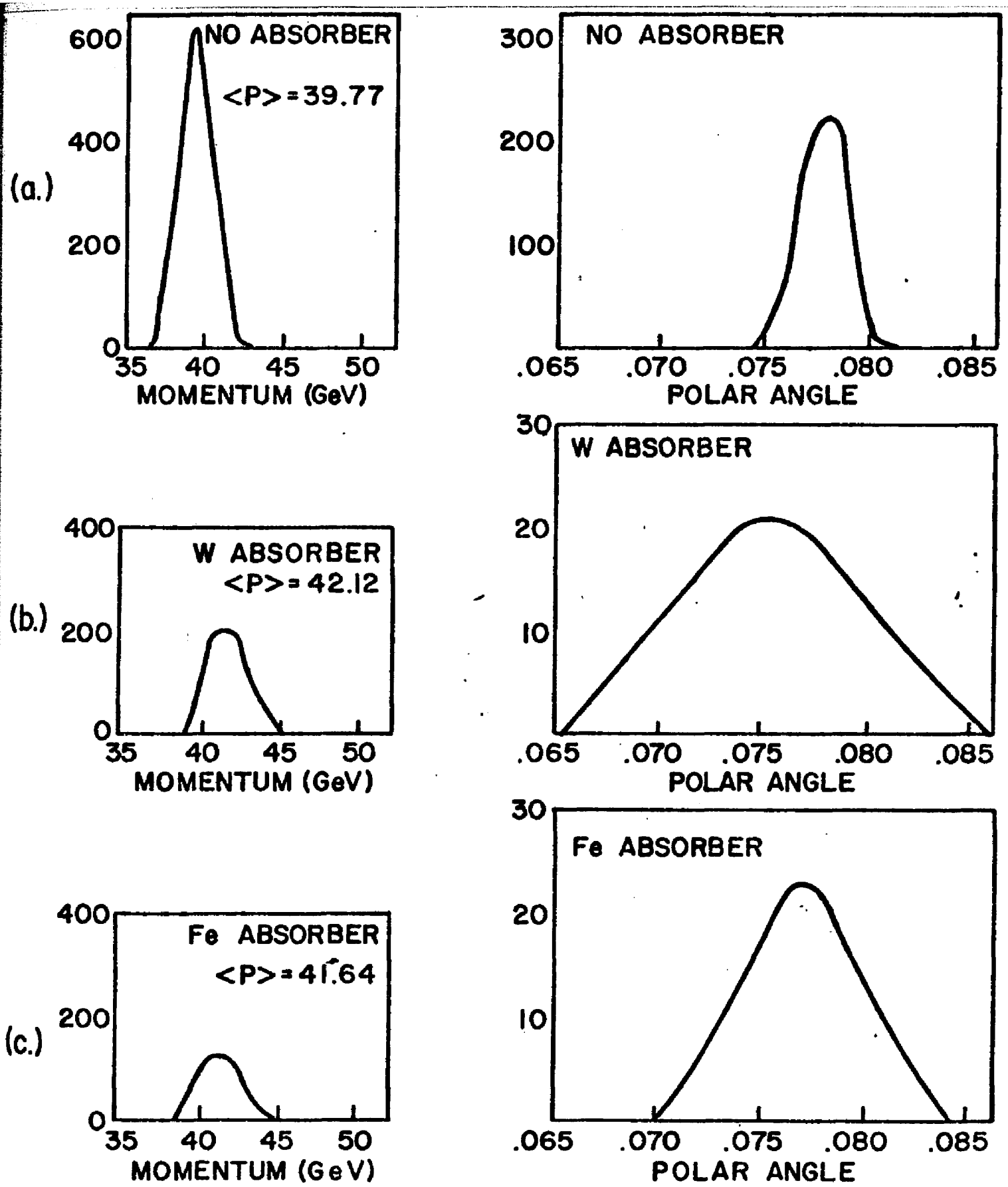

MONTE CARLO GENERATED ACCEPTANCE DISTRIBUTIONS FOR MAGNETIC ARM AS A FUNCTION OF MOMENTUM AND POLAR ANGLE FOR (a) NO ABSORBER, (b) W ABSORBER AND (c) Fe ABSORBER. VERTICAL AXIS IS RELATIVE PROBABILITY OF ACCEPTANCE INTO SPECTROMETER.

FIG. 3-8

The effect of the energy loss of muons traversing the absorber is to shift the mean momentum accepted by the spectrometer upwards by the amount lost in the absorber. If the production of muons at the target is described by:

$$E \frac{d^3\sigma}{d p^3} = K \quad e^{-\alpha P_T}$$

then the correction factor to be applied to the pions to normalize the muons measured at an increased average momentum is given by:

$$\frac{N_{p=p_0}}{N_{p=p_0+\Delta p}} = \frac{p^2 \; e^{-\alpha P \sin\theta}}{(p+\Delta p)^2 \; e^{-\alpha (p+\Delta p) \sin\theta}} = \frac{p^2 \; e^{\alpha \Delta p \sin\theta}}{(p+\Delta p)^2}$$

The correction factor derived in this manner is in good agreement with results from the Monte Carlo simulation of the energy loss which includes fluctuations.

The overall absorber correction factor calculated by a Monte Carlo program is defined as:

$$A'(p) = \frac{\text{acceptance with absorber out}}{\text{acceptance with absorber in}}$$

Plotted in figure 3-9 are these correction factors as a function of p_{spec} for both absorbers.

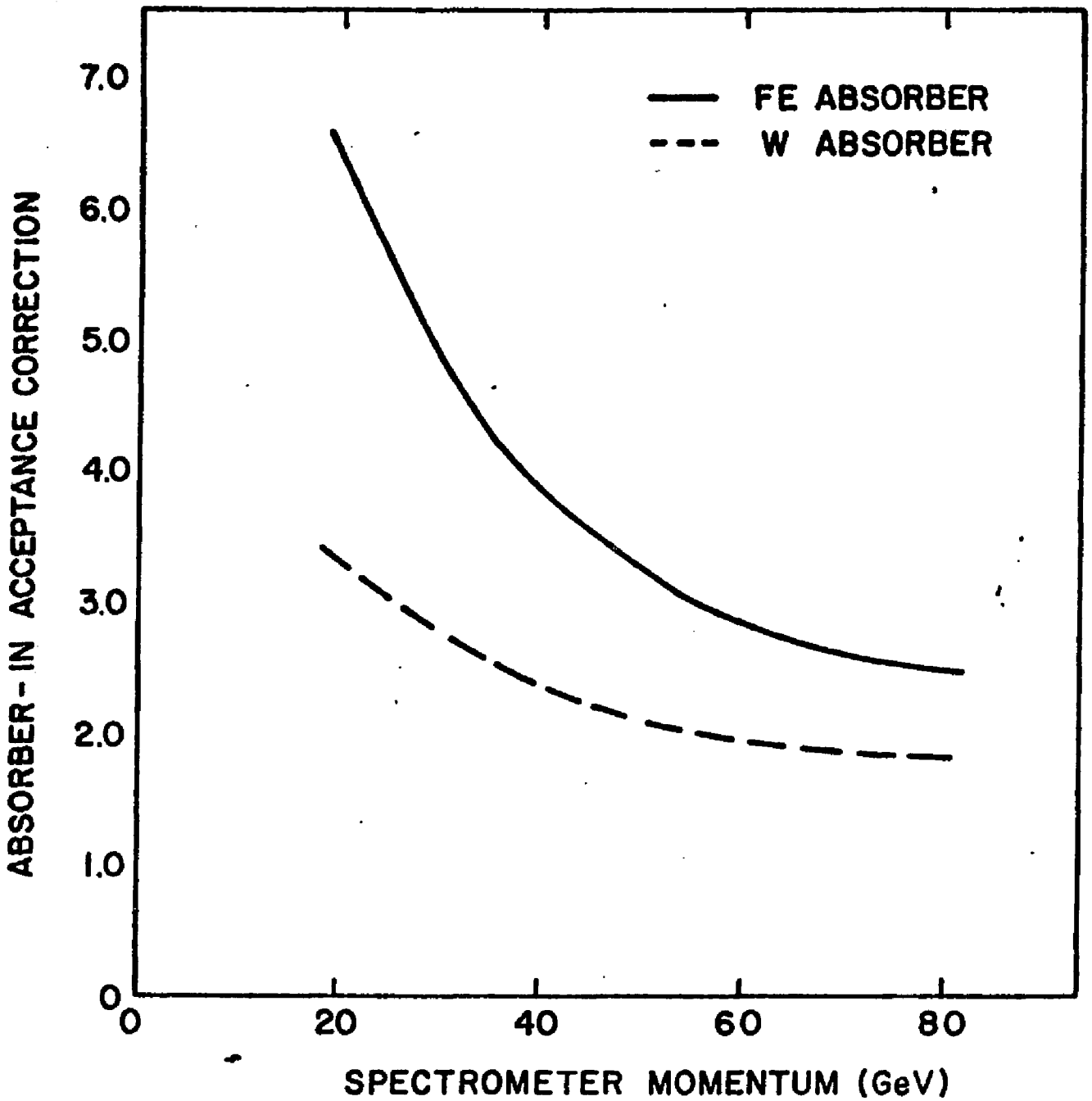

ACCEPTANCE CORRECTION FACTOR FOR ABSORBER-IN AS A FUNCTION OF SPECTROMETER MOMENTUM SETTING.

FIG. 3-9

In finding these corrections we assumed, a priori, that the P_T distribution for the production of muons was the same as for pions and checked this a postiori by comparing the calculated muon decay slope with that which we predict. We parameterized the pion cross section for use in the Monte Carlo generation of events as

$$E \frac{d^3\sigma}{dp^3} = B\, e^{-\alpha(P_T)\, P_T}$$

In summary, the corrected muon yield was calculated with :

$$\mu_i^{2,3} = \left(\mu_i^{1,2,3} - \frac{\mu_0}{\pi_0} \pi_i \right) A^i$$

Then normalized to the pion yield measured at the same momentum:

$$\left(\frac{\mu}{\pi}\right)_i = \frac{\mu_i / (90^\circ \text{ MONITOR})_i}{\pi_0 / (90^\circ \text{ MONITOR})_0} \frac{1}{S} \frac{1}{D} \frac{1}{T}$$

The experimental decay slope is then given by:

$$\Delta_{exp} = \frac{\left[\left(\frac{\mu}{\pi}\right)_{Fe} - \left(\frac{\mu}{\pi}\right)_W \right] \frac{1}{D} \frac{1}{T}}{d_1 - d_2}$$

where d_1 = distance to W Absorber
d_2 = distance to Fe Absorber

and finally we find the direct lepton yield at the target.

$$\left(\frac{\mu}{\pi}\right)_{TARGET} = \left(\frac{\mu}{\pi}\right)'_W - d_1 \Delta_{exp}$$

Figure 3-10 displays the decay slopes as calculated from the data as a function of P_T. They are in fair agreement with the predicted slopes as calculated by the formula above. An example of the extrapolation of μ/π to zero decay length is shown in figure 3-11,

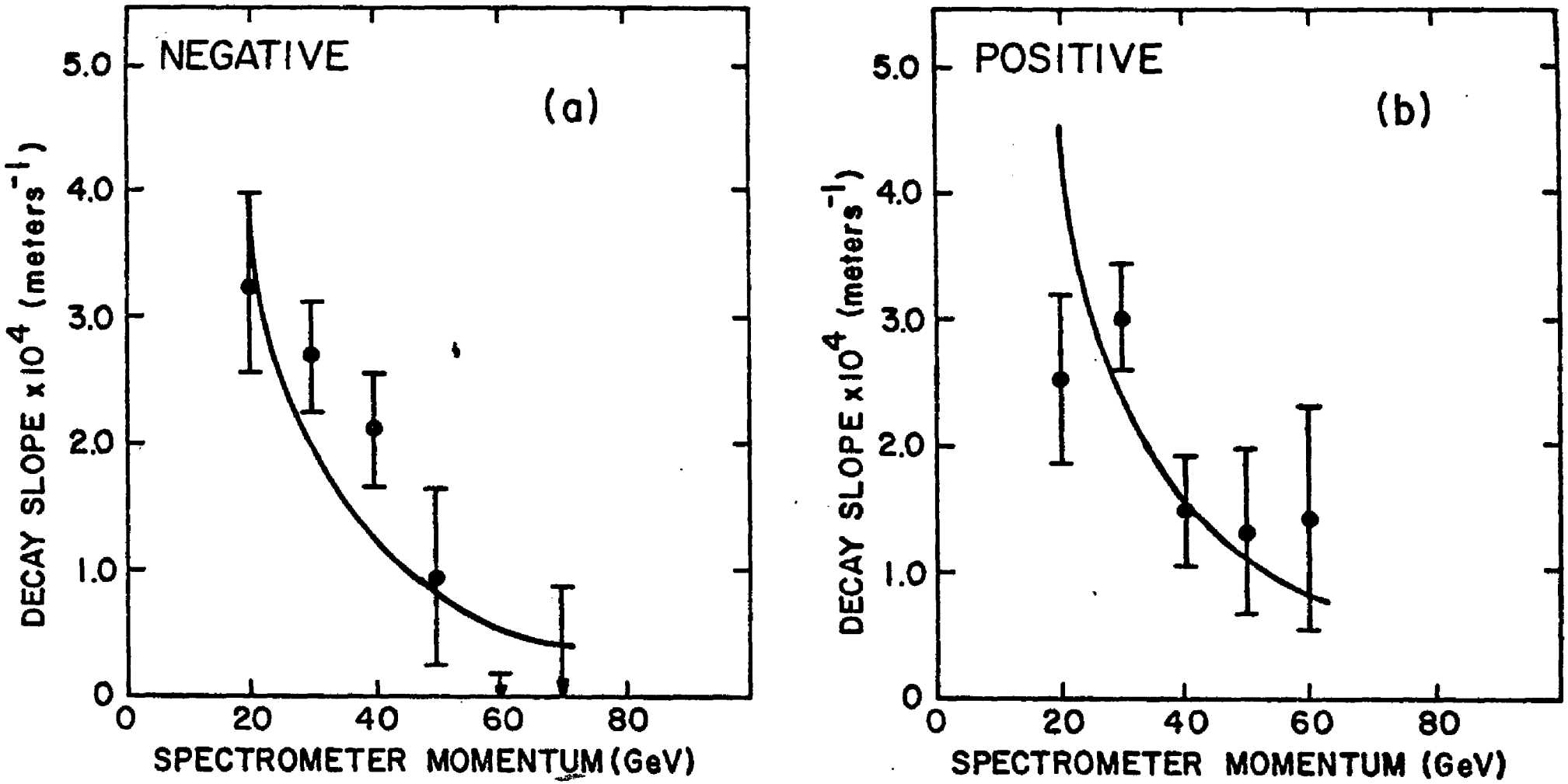

MEASURED AND CALCULATED DECAY SLOPES (NO. OF DECAYS/UNIT LENGTH) FOR (a) μ^- DATA, AS A FUNCTION OF SPECTROMETER MOMENTUM.

FIG. 3-10

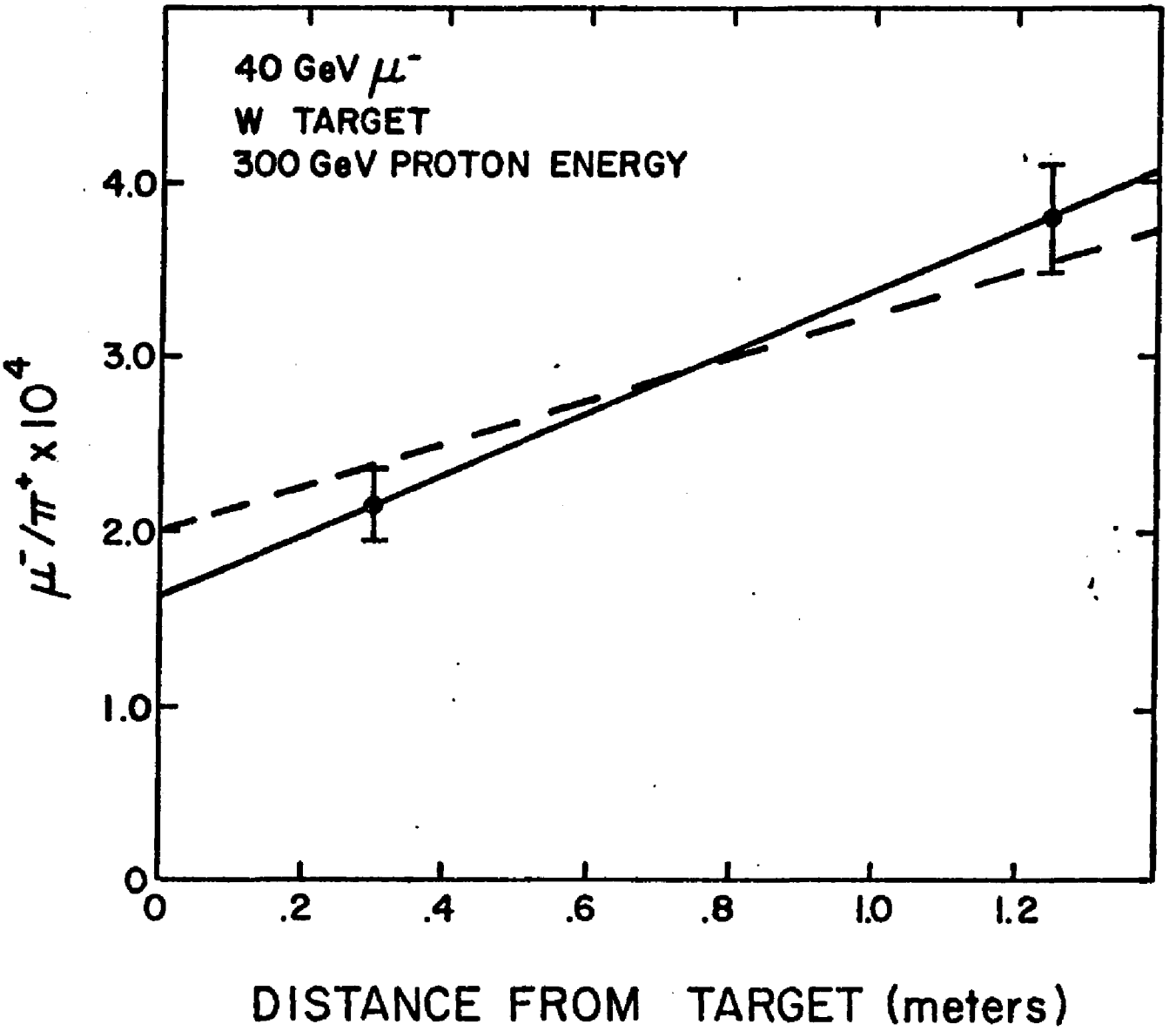

EXTRAPOLATION OF 40 GeV MEASUREMENTS TO ZERO DECAY LENGTH TO OBTAIN μ/π AT TARGET. SOLID LINE IS LINEAR EXTRAPOLATION, DASHED LINE IS PREDICTED SLOPE.

FIG. 3-11

along with the expected slope fit to the two data points.

ELECTRON ANALYSIS

Data were taken with the incident proton beam located at three different transverse positions on the target (see Chapter 2) This was done in order to eliminate the background electrons by extrapolation of the yields to a negative conversion length. The systematic corrections fall into three categories:

1) Reconstruction efficiencies

2) Acceptance corrections

3) Subtraction of background from π^0 and η decays.

The main sources of background electrons are conveniently divided into two groups to be treated differently in the analysis.

1) electrons produced downstream of the interaction point (external conversion)

a) π^0 decay photons

b) η decay photons

2) electrons produced at the interaction point.

a) direct electrons

b) Dalitz pairs

(i) π^0 Dalitz

(ii) η Dalitz

RECONSTRUCTION INEFFICIENCIES

While measuring electron yields the apparatus was rate limited by accidentals in the first hodoscope. Each hodoscope could record only one hit per R.F. bucket. During the run the accidentals in H1 were constantly monitored by observing the accidentals in an A1* A2 coincidence. A1*A2 accidentals were required to be less than 15%. This resulted in the overall reconstruction efficiencies shown below:

Targeting Position	Reconstruction Efficiency
0 mm	94.3%
1 mm	90.6%
3 mm	89.5%

ACCEPTANCE CORRECTIONS

The electrons lose energy through bremsstrahlung when traversing the target and material in the spectrometer. A Monte Carlo program was written to correct for the loss of electron acceptance caused by this effect. Conversion electrons and electrons produced at the interaction point required different corrections.

Externally converted electrons could be produced anywhere along the secondary beam line before the first bend. Direct and Dalitz decay electrons are all assumed to be produced at the interaction point.For this reason different acceptance corrections were needed for these two sources of electrons. Appendix I lists the number of conversion lengths of each type of material in the secondary beam line.

The background electrons and the direct electrons were assumed to be produced with different transverse momentum distributions. This must also be taken into account when deriving the acceptance corrections. The direct electrons were assumed to have the transverse momentum distribution:

$$N_e^{direct} \propto P_T \, e^{-\alpha(P_T)\, P_T} \, dP_T$$

as were the direct muons. On the other hand, the electrons resulting from π^0 and η decay were assumed to be produced according to:

$$N_e^{decay} \propto \frac{e^{-\alpha(P_T)\, P_T}}{P_T} \, dP_T$$

The two major effects explained above contribute with opposite signs. The steeper transverse momentum distribution of the background electrons allows them to be more easily lost from the spectrometer given the same energy loss. The production of all direct electrons at the interaction point means that they lose more energy traversing the spectrometer. The latter effect is the main contribution at larger conversion lengths. This means the acceptance for externally converted photons is larger then for direct electrons.

The electron correction factors are plotted in figure 3-12. The corrections are a function of the amount of converter, x, between the interaction point and the first bend. They are defined in the following manner:

$$A(x) = \frac{\text{electron acceptance(bremsstrahlung turned on)}}{\text{electron acceptance(bremsstrahlung turned off)}}$$

SEPARATION OF THE ELECTRON SIGNAL

In order to apply the corrections discussed in the preceeding section one needs to know the composition of the measured electron yield.

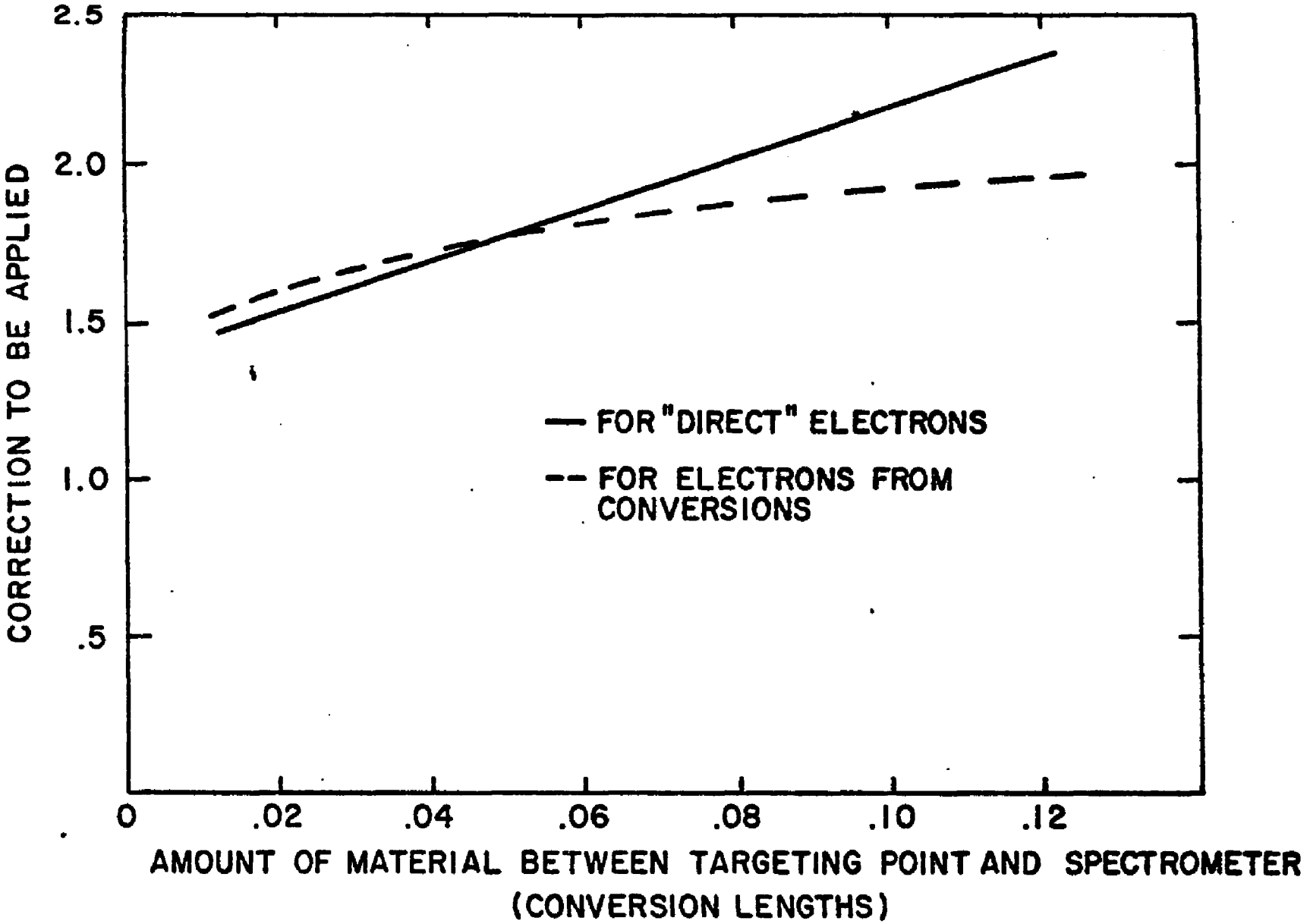

ELECTRON MONTE CARLO ACCEPTANCE CORRECTION FACTORS AS A FUNCTION OF THE AMOUNT OF MATERIAL BETWEEN THE TARGETING POINT AND THE SPECTROMETER.

FIG. 3-12

The corrected electron yield, N^i_{ce}, is given by:

$$N^i_{ce} = A^i N_t^i + B^i (N_e - N_t^i) \qquad i = 1,3 \qquad (3.1)$$

where:

i = index which identifies amount of converter

N_t^i = raw electron yield due to direct and Dalitz decay sources

N_e^i = raw electron yield due to conversion electrons

A^i = M.C. correction for direct electrons

B^i = M.C. correction for conversion electrons

The corrected N_t^i are independent of the conversion length.

$$A^i N_t^i = N_{dir}, \text{ for } i = 1,3 \qquad (3.2)$$

Substituting (3.2) into (3.1) we have :

$$N^i_{ce} = (1 - B^i / A^i) N_t + B^i N_e^i \qquad (3.3)$$

Now, we impose the requirement that the converted electron yields are a linear function of the conversion length, x^i.

$$Y^i = N_t + (dn/dx) x^i \qquad (3.4)$$

N_t, dn/dx, and N^i_{ce} are found by determining the N_t and dn/dx which minimized:

$$\chi^2 = \sum_{i=1}^{3} \frac{[Y^i - N^i_{ce}]^2}{\sigma^2_{N^i_{ce}}}$$

The final result is shown in figure 3-13. The straight-line fit is extrapolated to $X = -6.22 \times 10^{-3}$ to eliminate the Dalitz background from π^0 and η decays (Appendix II).

We have considered the contribution to the direct electron signal from the semi-leptonic decay of strange particles. These sources are found to be negligible. As an example, the contribution due to K_{e3} decay is calculated to be

$$\frac{N_e^{K_{e3}}}{N_\pi} \lesssim 5 \times 10^{-6}$$

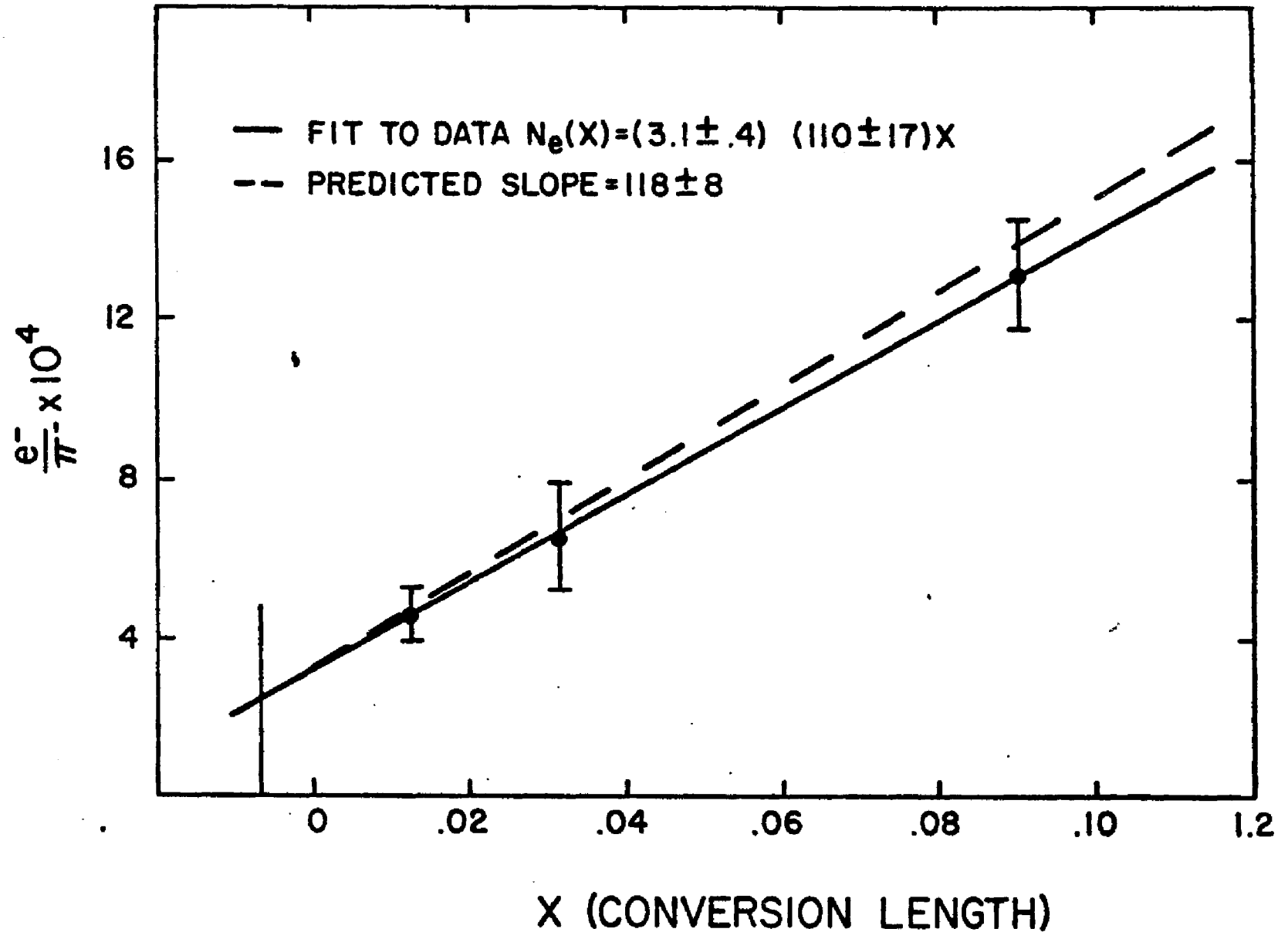

CORRECTED ELECTRON YIELD AS A FUNCTION OF THE AVERAGE AMOUNT OF MATERIAL BETWEEN THE TARGETING POINT AND THE SPECTROMETER (X).

FIG. 3-13

CHAPTER 4

RESULTS

In this chapter results are presented and the main features of the data are discussed. Interpretations of the data are given in terms of models of production for the various parents of the leptons.

SINGLE MUONS

Table 4-1 displays the results obtained for the measurement of the ratio lepton/π. The ratio is given for the various targets, lepton type, incident energies and transverse momentum for which data were taken. The inclusive muon cross-sections are given in table 4-2.

The constancy of the muon cross-section with respect to the pion cross-section is shown in figure 4-1. Here we plot the muon cross-section along with the pion cross-section $\times 10^{-4}$. The change in the μ/π ratio as a function of transverse momentum is small in comparison to the change in the absolute cross-sections.

Target	μ^-/π^- ($\times 10^4$)					μ^+/π^+ ($\times 10^4$)			e^-/π^- ($\times 10^4$)
	Be	Cu			W	Be	Cu	W	Be
Proton Energy (GeV) / P_T (GeV)	400	200	300	400	300	300	300	300	400
1.54					1.46±.17		1.73±.31		
2.31					1.10±.22		1.23±.20		
3.08			1.64±.26	1.52±.10	1.42±.26	1.72±.29	1.77±.25	1.05±.22	
3.85		1.72±.12	1.93±.16	2.04±.13	1.69±.41		1.95±.38		
4.62	3.97±.24*	1.73±.17*		2.17±.30	2.20±.58*		1.60±48		2.45±.45
5.01			2.66±.50						
5.39				2.67±.53	2.75±91*		2.28±97*		
5.78			3.55±50*						
6.16				2.39±.50					

TABLE 4.1 Summary of Direct Lepton Results.
Ratio ℓ/π

* INDICATES DATA WERE TAKEN WITH W-ABSORBER ONLY.

$E \frac{d^3\sigma}{dp^3}$ FOR μ^- (cm^2/GeV^2/nucleus)

TARGET	Be	Cu			W
PROTON ENERGY (GeV)	400	200	300	400	300
P_T (GeV/c)					
1.54					4.86×10^{-31} ±.57
2.31					2.01×10^{-32} ±.40
3.08			5.41×10^{-34} ±.86	7.89×10^{-34} ±.52	1.53×10^{-33} ±.28
3.85		1.37×10^{-35} ±.10	4.63×10^{-35} ±.38	8.32×10^{-35} ±.53	1.31×10^{-34} ±.32
4.62	1.50×10^{-36} ±.09	7.42×10^{-37} ±.73		7.79×10^{-36} ±1.08	1.40×10^{-35} ±.37
5.01			1.27×10^{-36} ±.24		
5.39				1.03×10^{-36} ±.20	1.52×10^{-36} ±.50
5.78			1.71×10^{-37} ±.24		
6.16				1.02×10^{-37} ±.21	

$E \frac{d^3\sigma}{dp^3}$ FOR μ^+ (cm^2/GeV^2/nucleus)

Be	Cu	W
300	300	300
	2.28×10^{-31} ±.41	
	8.46×10^{-33} ±1.38	
7.50×10^{-35} ±1.26	6.48×10^{-34} ±.92	1.24×10^{-33} ±.26
	5.44×10^{-35} ±1.06	
	3.41×10^{-36} ±1.02	
	4.54×10^{-37} ±1.93	

Table 4-2 Summary of inclusive muon cross-sections.

$E \frac{d^3\sigma}{dp^3}$ FOR μ^- (cm^2/GeV^2/nucleon)

TARGET	Be	Cu			W
PROTON ENERGY (GeV)	400	200	300	400	300
P_T (GeV/c)					
1.54					$2.64 \times 10^{-29} \pm .31$
2.31					$1.09 \times 10^{-30} \pm .22$
3.08			$8.51 \times 10^{-32} \pm 1.35$	$1.24 \times 10^{-31} \pm .082$	$8.32 \times 10^{-32} \pm 1.52$
3.85		$2.15 \times 10^{-33} \pm .16$	$7.29 \times 10^{-33} \pm .598$	$1.31 \times 10^{-32} \pm .083$	$7.13 \times 10^{-33} \pm 1.74$
4.62	$1.66 \times 10^{-33} \pm .10$	$1.16 \times 10^{-34} \pm .11$		$1.23 \times 10^{-35} \pm .17$	$7.61 \times 10^{-34} \pm 2.01$
5.01			$2.00 \times 10^{-34} \pm .38$		
5.39				$1.62 \times 10^{-34} \pm .31$	$8.27 \times 10^{-35} \pm 2.72$
5.78			$2.69 \times 10^{-35} \pm .37$		
6.16				$1.61 \times 10^{-35} \pm .33$	

$E \frac{d^3\sigma}{dp^3}$ FOR μ^+ (cm^2/GeV^2/nucleon)

Be	Cu	W
300	300	300
	$3.59 \times 10^{-29} \pm .65$	
	$1.33 \times 10^{-30} \pm .22$	
$8.32 \times 10^{-32} \pm 1.40$	$1.02 \times 10^{-31} \pm .19$	$6.74 \times 10^{-32} \pm 1.41$
	$8.56 \times 10^{-33} \pm 1.61$	
	$5.37 \times 10^{-34} \pm 1.61$	
	$7.14 \times 10^{-35} \pm 3.04$	

Table 4-3 Summary of inclusive muon cross-sections extrapolated to A=1.

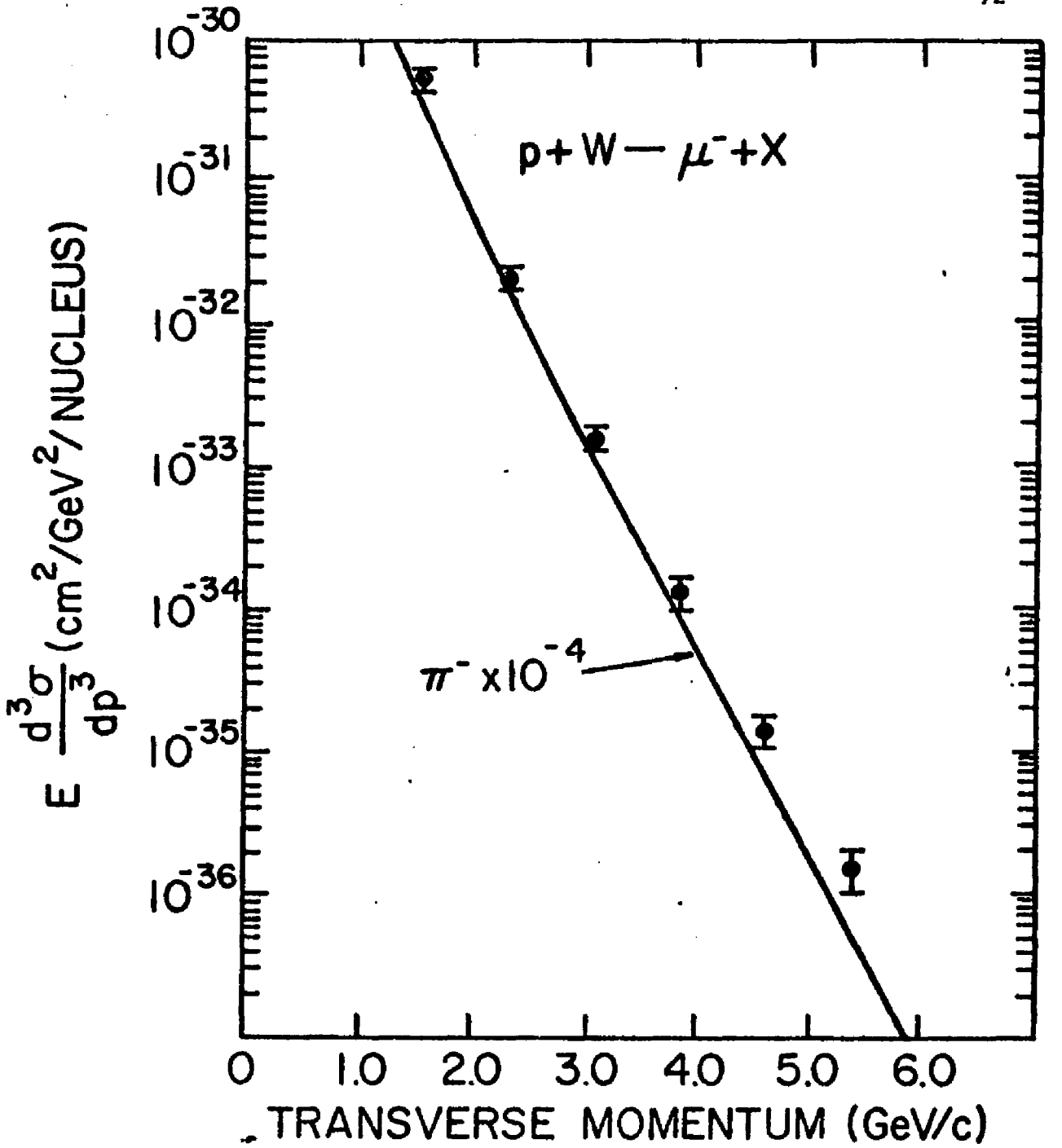

DATA POINTS ARE MEASURED μ^- INCLUSIVE CROSS-SECTION FOR 300 GeV PROTONS ON A W TARGET. THE SOLID LINE IS THE PION CROSS-SECTION $\times 10^{-4}$.

FIG. 4-1

The μ/π ratio as a function of transverse momentum is plotted in figure 4-2 for the various conditions for which data were taken. All show a noticeable rise at higher p_T with the possible exception of the positive data. We attribute the difference in behavior of the μ^+/π^+ at high P_T to a change in the π^+/π^- ratio and not a difference in the production rate of oppositely charged muons. When comparing the muon cross-sections(table 4-3) there is no statistically significant difference between the μ^+ data and the μ^- data.

For the point at P_T=3.08 GeV data were taken with 3 different targets. The A-dependence of the muon cross-section is shown in figure 4-3. The data are consistent with linear A dependence. This was the assumption used in obtaining the muon cross-sections extrapolated to A=1 (table 4-3).

The μ/π ratio is plotted as a function of $\sqrt{s}$ in figure 4-4 at P_T=3.85. A linear fit gives:

$$\mu/\pi = (1.34\pm.28) + (.021\pm.01)\sqrt{s}] \times 10^{-4}$$

Our value of the slope is in agreement with the results of Büsser et al.[18]. They find for electrons produced with P_T between 1.5 and 3.5 GeV :

$$e/\pi = [\ (.27\pm.22) + (.0144\pm.004)\sqrt{s}\ ] \times 10^{-4}$$

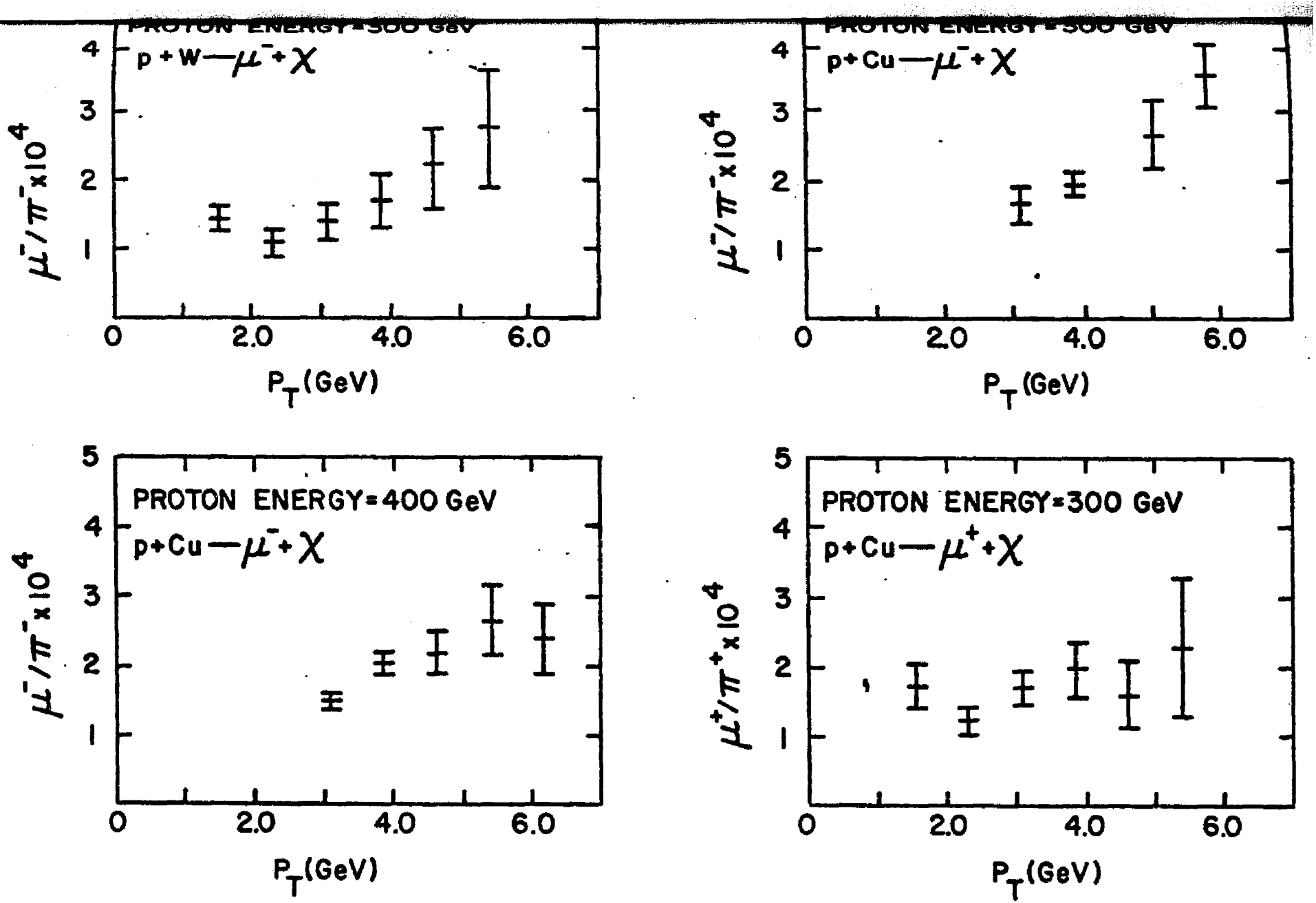

THE RATIO μ/π AS A FUNCTION OF TRANSVERSE MOMENTUM.

FIG. 4-2

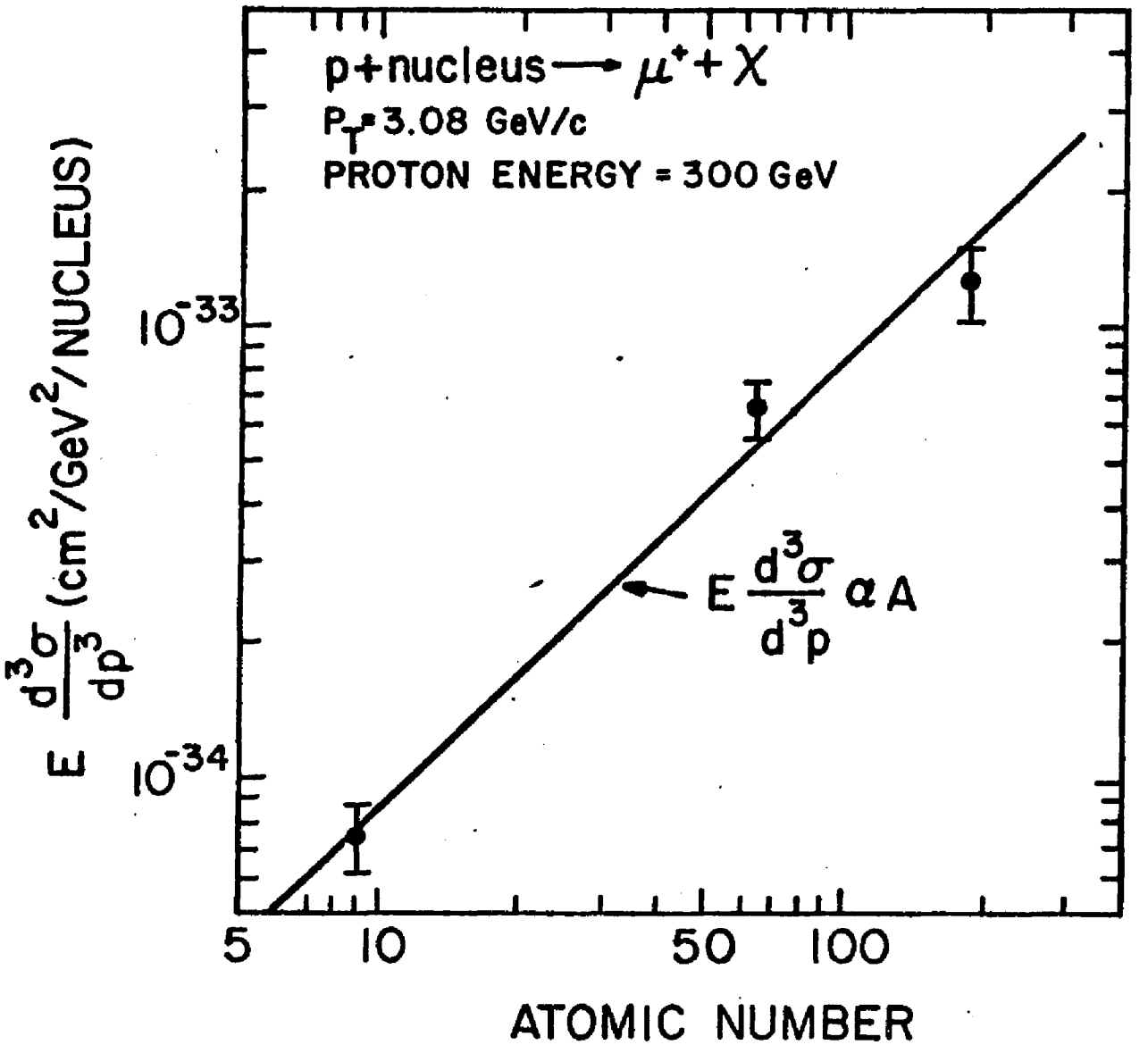

ATOMIC NUMBER DEPENDENCE OF SINGLE MUON CROSS-SECTION AT P_T=3.08 GeV/c. DATA TAKEN WITH W, Fe, AND Be TARGETS.

FIG. 4-3

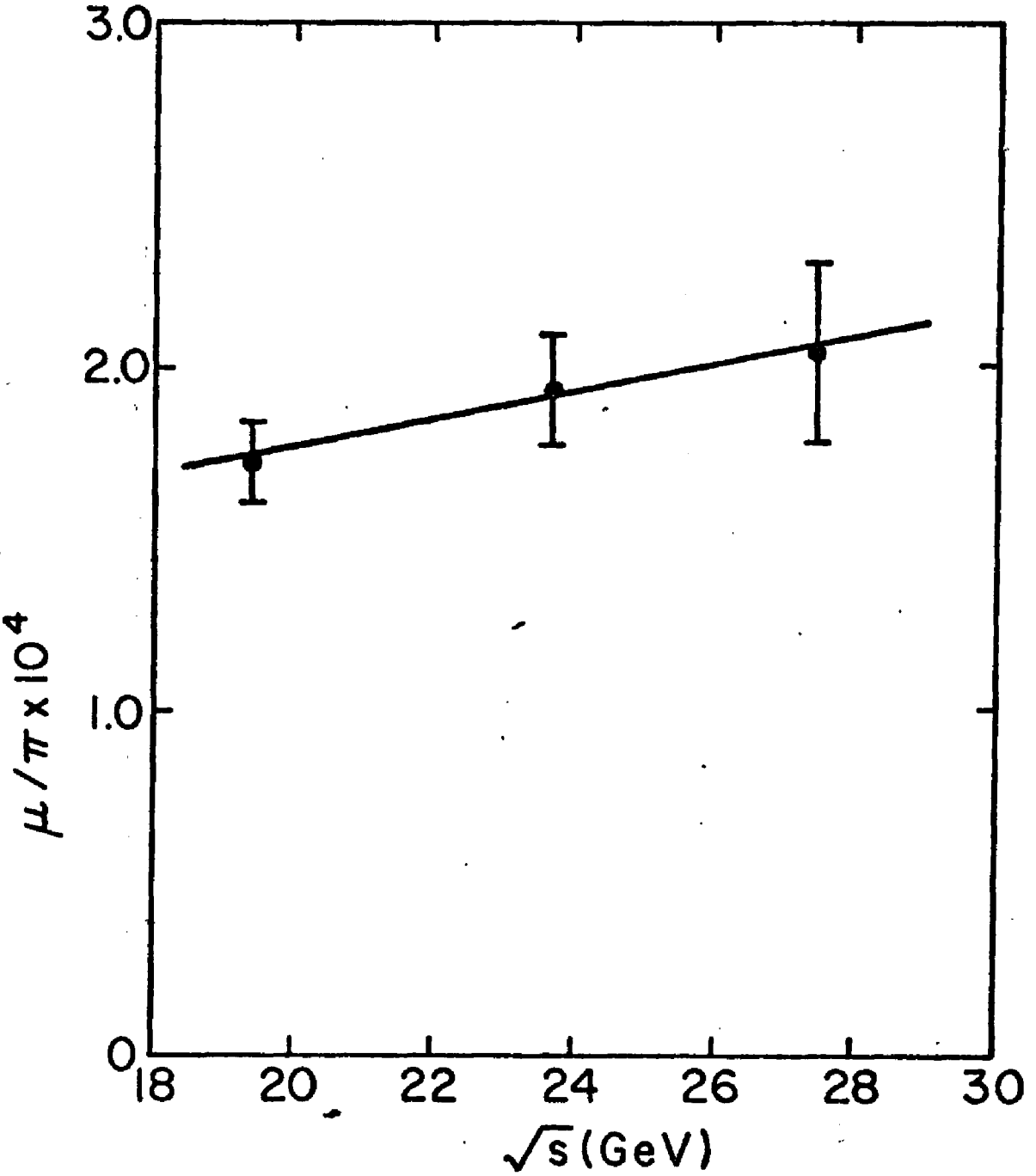

μ/π AS A FUNCTION OF PROTON-NUCLEON CENTER OF MASS ENERGY AT $P_T = 3.85$ GeV/c

FIG. 4-4

To examine more closely the behavior of μ/π as a function of transverse momentum, all 300 GeV muon cross-sections measured at the same p_T were extrapolated to A=183.85 and normalized by the π^- yield measured on tungsten. Tungsten was chosen because the pion spectrum was best measured on this target. In the extrapolation to tungsten a linear A dependence was assumed. The result is plotted in figure 4-5.

Contribution of J/Ψ and Υ to the Single Muon Yield

In figure 4-6 are shown contributions of the J/Ψ to the single muon yield for various production models of the J/Ψ. The models used were:

(1.) exponential:

$$E\frac{d^3\sigma}{dp^3} = A\, e^{-bp_T}(1-|x|)^a$$

(2.) gaussian:

$$E\frac{d^3\sigma}{dp^3} = B\, \exp(-bp_T^2)\ (1-|x|)^a$$

(3.) Bourquin and Gaillard model[12]

$$E\frac{d^3\sigma}{dp^3} = C\,\frac{2^{12.5}}{E_t+2}\,\exp(-5.13/Y^{.38})$$

$$\times \begin{cases} e^{-p_T}, & P_T < 1\ \text{GeV/c} \\ e^{-23(p_T-1)/\sqrt{s}}e^{-1}, & P_T > 1\text{GeV/c} \end{cases}$$

where $Y = (E^{max} + P_L^{max}) / (E + P_L)$

The distibutions are very sensitive to the slope of the P_T distribution,b. Using distributions (1.),and (2.) to predict J/ψ

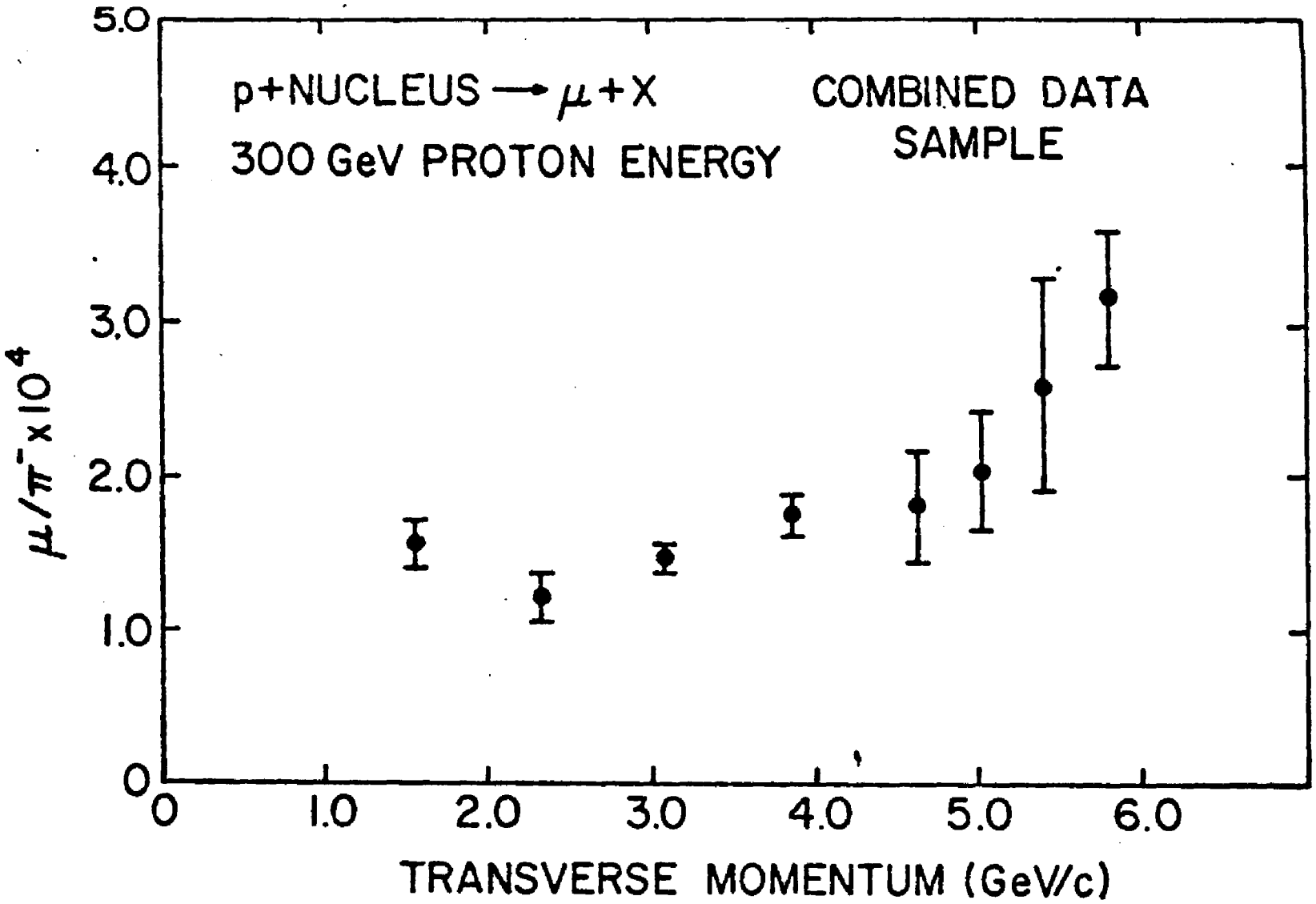

ALL 300 GeV μ^+ AND μ^- DATA COMBINED AND NORMALIZED BY π^- YIELD

FIG.4-5

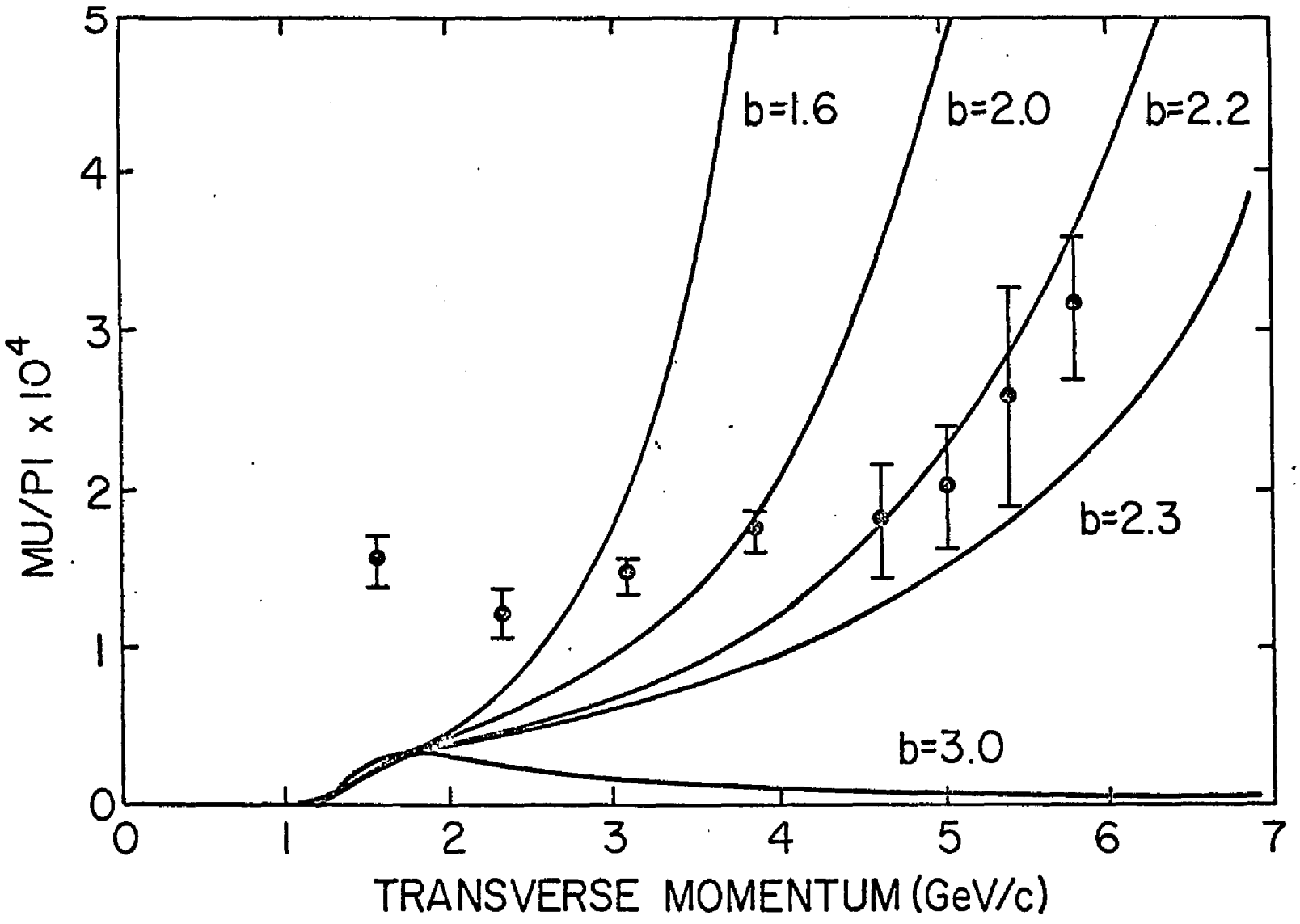

J/ψ CONTRIBUTION TO SINGLE MUON YIELD USING EXPONENTIAL MODEL FOR VARIOUS VALUES OF PARAMETER b.

FIG. 4-6(a)

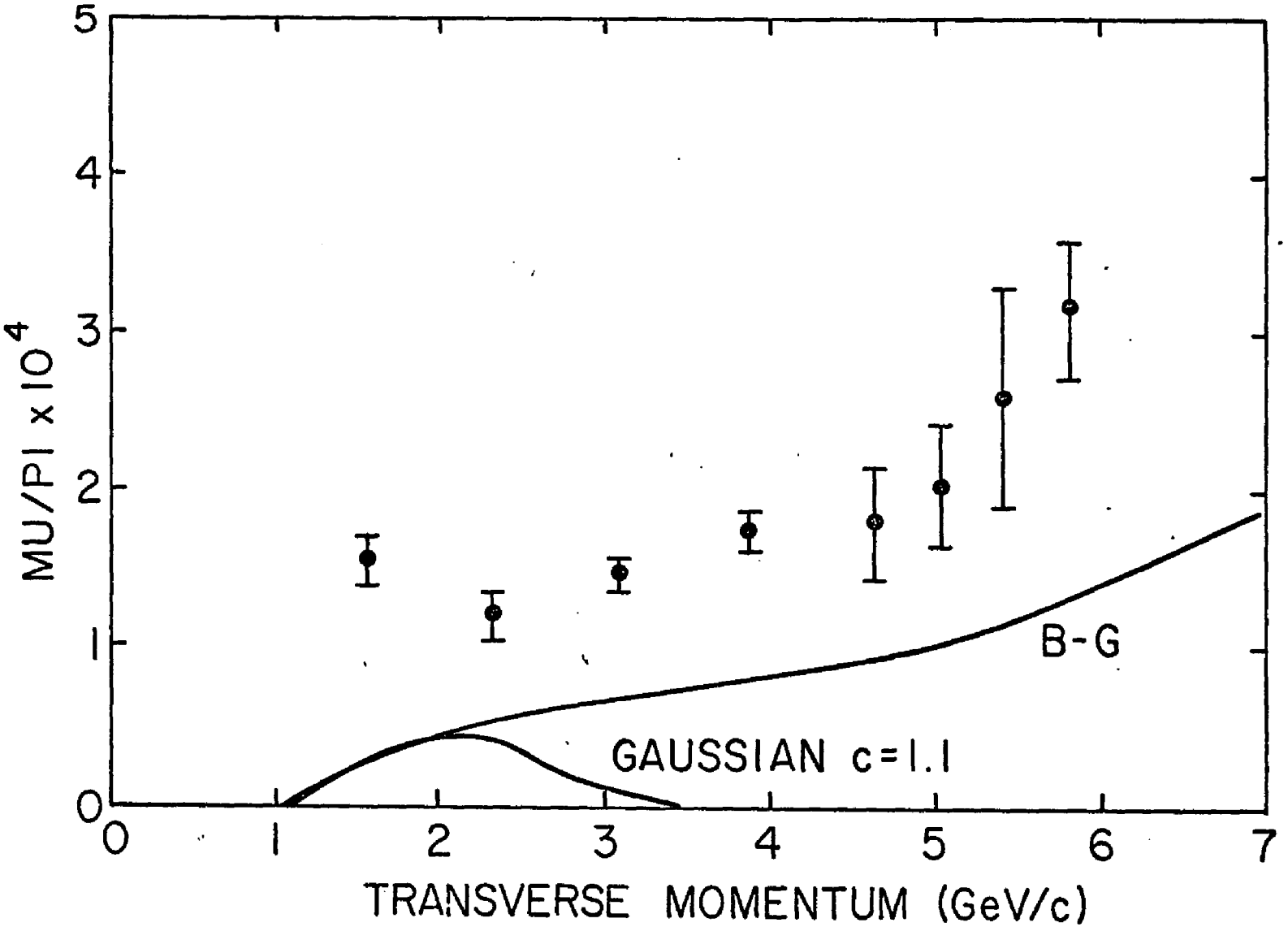

J/ψ CONTRIBUTION TO SINGLE MUON YIELD FOR B-G MODEL AND GAUSSIAN MODEL WITH C.F.S. VALUE FOR PARAMETER c.

FIG. 4-6(b)

contributions to the single muon spectrum relies on knowing the p_T distributions for the production of J/ψ out to p_T=6 GeV/c. Since this has only been measured out to p_T=2.5 GeV/c[19], an extrapolation is necessary. The values found to fit data in the Columbia-Fermilab-Stony Brook(CFS) experiment in the range P_T=0.0 to p_T=2.5 GeV/c were:

exponential:

$$\frac{d^3\sigma}{dp^3} = A\ e^{-bp_T} \qquad ;\ b=1.6 \pm .35\ \mathrm{GeV}^{-1}$$

gaussian:

$$E\frac{d^3\sigma}{dp^3} = B\ e^{-cp_T} \qquad ;\ c = 1.1 \pm .35\ \mathrm{GeV}^{-2}$$

The expected contribution from the exponential model with the CFS fit is shown in figure 4-6(a.) along with the contribution expected assuming other values of the parameter b. Clearly b=1.6 is too large to accommodate the data at large P_T. The gaussian model is shown in figure 4-6(b.).

If we take another approach and assume all the single muons in the region p_T>3 GeV/c arise from J/ψ and in addition assume a exponential model for the p_T distribution we find:

$$E\frac{d^3\sigma}{dp^3} = A\ e^{-bp_T} \qquad ;b= 2.2 \pm .1$$

best fits the data.

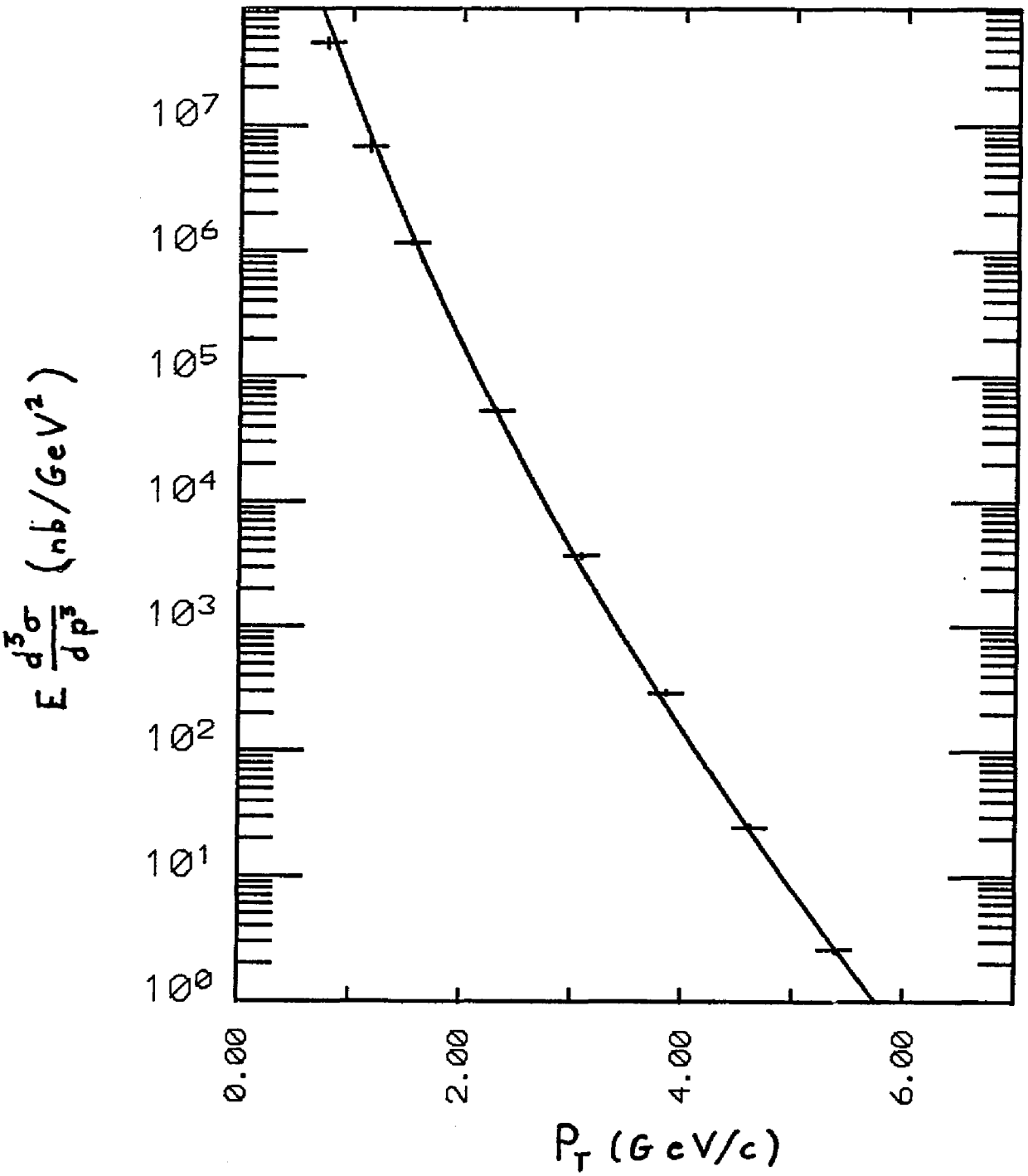

COMPARISON OF π^- INCLUSIVE CROSS-SECTION WITH B-G PRODUCTION SPECTRUM.

FIG. 4-7

The model of Bourquin and Gaillard is especially appealing since it does fit the production spectrum of other particle types at high p_T. Its parameters were fit to a large base of data some of which included data taken by this group. As an example, figure 4-7 compares our pion data on a tungsten target with the B-G parameterization. The agreement is excellent. The J/ψ contribution to the single muon yield calculated using the B-G model is shown with the data in figure 4-6(b.). Here we see the J/ψ contributes at a significant level even at the highest P_T. Using this same model the Υ contribution was calculated and is shown in figure 4-9.

Contribution of Dimuons to Single Muon Yield

For a subset of the data the fraction of direct muons which were accompanied by a muon in the second arm was measured. The results are tabulated in table 4-4. Using these data along with a knowledge of the production spectrum of the parent dimuon the contribution of the dimuon continuum to the single muon yield is derived (figure 4-8). The assumed production parameters were obtained from the results of Yoh et al.[28] and Branson et al.[21]

$$E \frac{d\sigma}{dM} = A\, e^{-kM}$$

$$E \frac{d^3\sigma}{dp^3} = B \exp(-2p_T / \bar{p}_T)\ (1 - x)^{4.3}$$

where $\bar{P}_T$ was measured as a function of the dimuon mass.

P_{INC} / P_T (GeV/c)	200 GeV/c	300 GeV/c	400 GeV/c
3.85	1.03 ± .20 %	1.04 ± .22 %	1.1 ± .20 %
4.62	2.95 ± .80 %	5.13 ± .81 %	5.20 ± .47 %
5.01		6.84 ± 1.2 %	
5.39			11.8 ± 2.1 %
5.78		17.4 ± 3.7 %	
6.01			14.8 ± 4.6 %

Percentage of single muons which were accompanied by a muon in the MHS (uncorrected).

TABLE 4-4

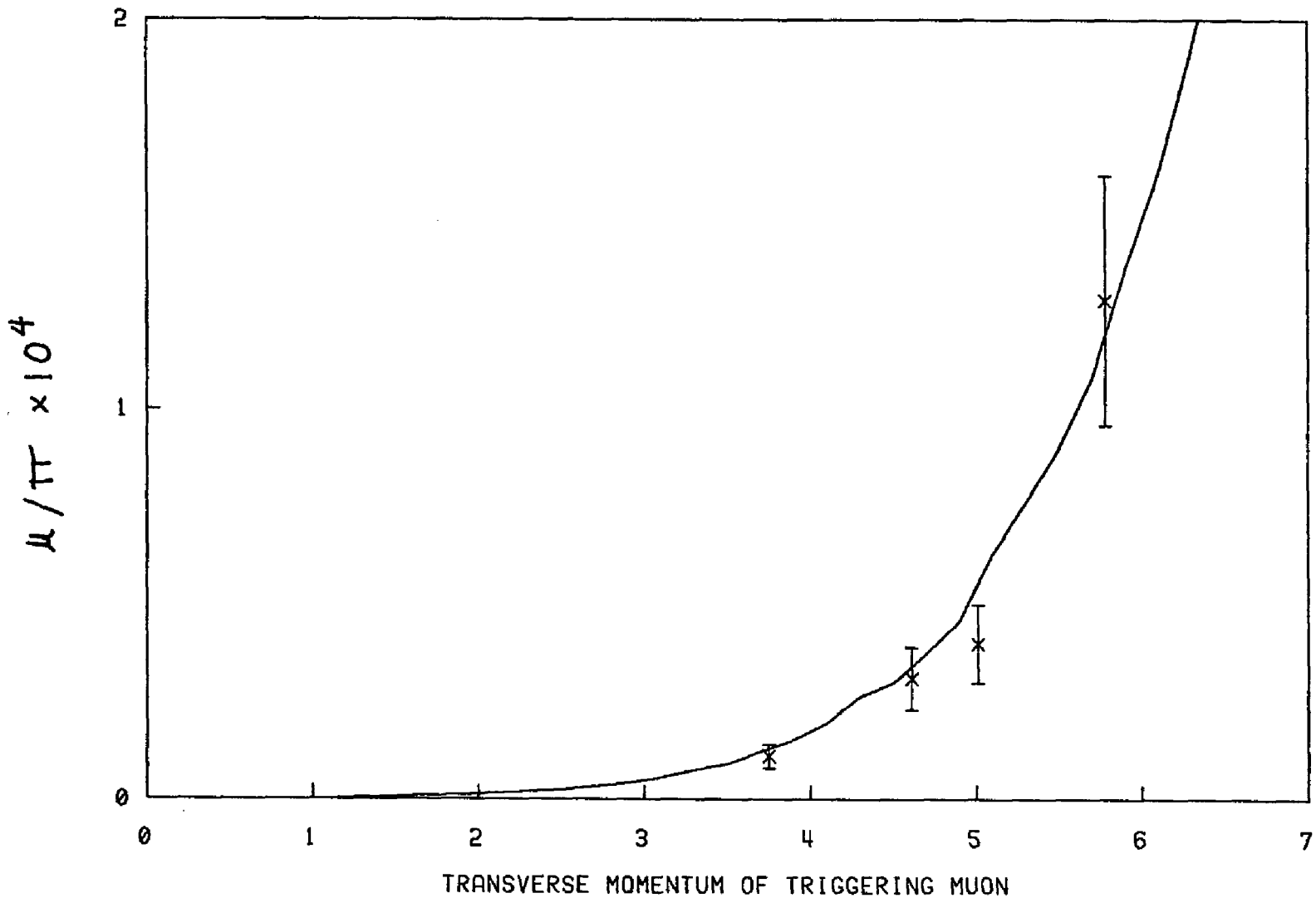

MEASURED DIMUON CONTRIBUTION TO SINGLE MUON YIELD COMPARED WITH PREDICTED CONTRIBUTION.

FIG. 4-8

The overall normalization was obtained by requiring that:

$$\frac{\left.\dfrac{\mu\,\mu}{\mu_{all}}\right|_{observed}}{\left.\dfrac{\mu\,\mu}{\mu_{\mu\mu}}\right|_{predicted}} \qquad \left.\frac{\mu_{all}}{\pi}\right|_{observed} = \left.\frac{\mu_{\mu\mu}}{\pi}\right|_{predicted}$$

Here the "predicted" values are the Monte Carlo generated values with the production spectrum, and mass spectrum given above. The observed values were measured in this experiment. The agreement between the predicted and observed values is remarkable as displayed in figure(4-12). The sum of all the contributions discussed is shown in figure 4-8.

The total contribution from J/ψ, Υ, and continuum dimuon production is shown in figure 4-9. TheJ/ψ and Υ contributions were both obtained with the B-G parameterization discussed above. The Υ production cross-section was obtained by extrapolating the results of Ueno et al.[22] at $\sqrt{s} = 27.4$ to $\sqrt{s} = 23.7$. The contribution is small because of the small amount of C.M. energy available. At higher energies, such as at ISR, we could expect the Υ to contribute at a much higher level.

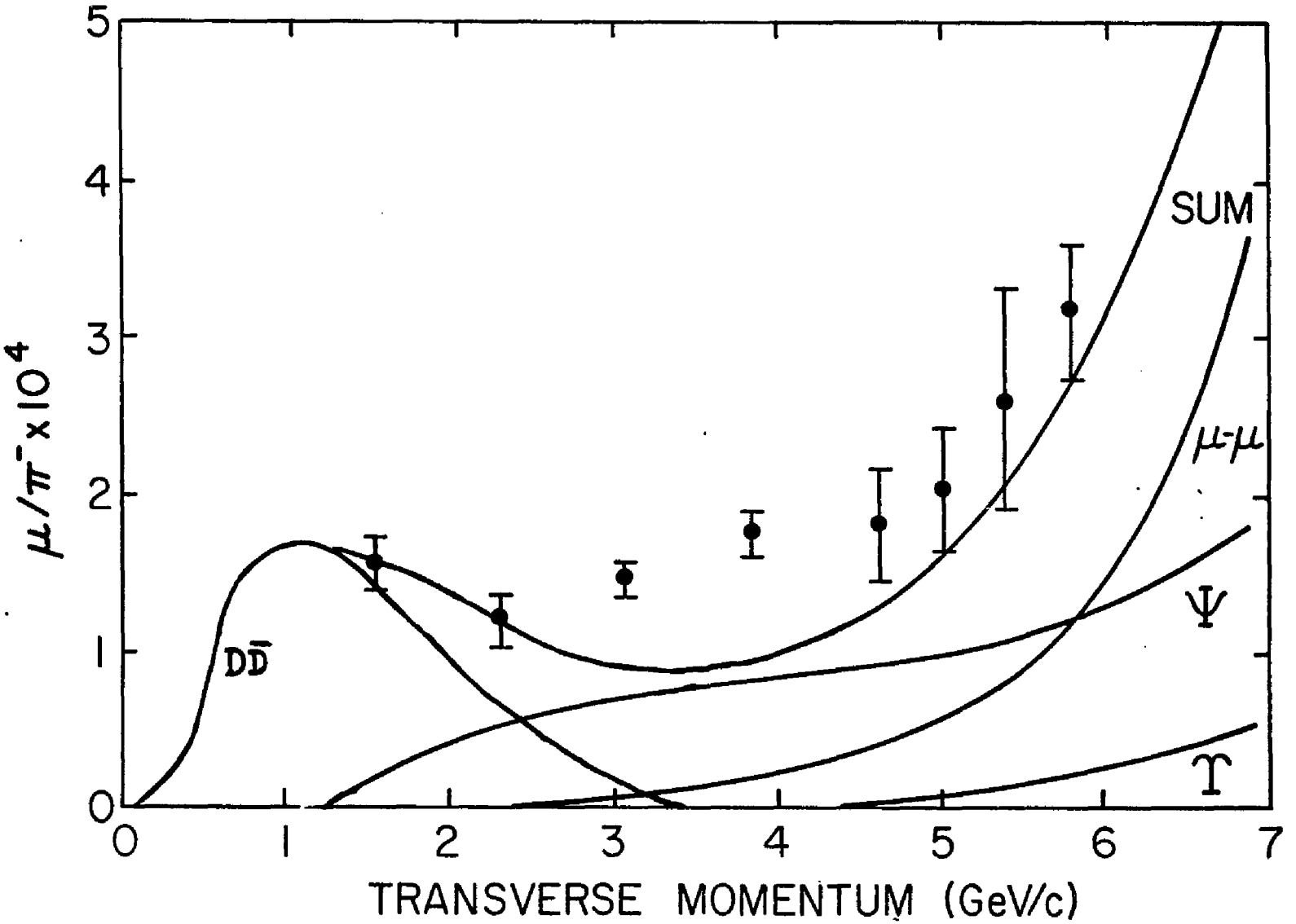

SUM OF J/Ψ, Υ, DIMUON and $D\bar{D}$ CONTRIBUTION TO SINGLE MUON YIELD. B-G MODEL ASSUMED FOR PRODUCTION OF J/Ψ AND Υ.

FIG. 4-9

Contribution of Charm and Bottom Mesons to the Single Muon Yields

The contributions of charm meson decay and bottom meson decay differ from the previous particles discussed in that they contribute at lower transverse momentum. The procedure is very nearly the same as with the other parents of the muons in that we have to assume the production spectrum for the parent particle. In the case of charm though, limits have been established on the parameters of the production distribution by Brown et al.[13] since they can distinguish between single and double muon events. Their data are consistent with the distribution,

$$E\frac{d^3\sigma}{dp^3} = C(1-|x|)^{\beta} e^{-\alpha P_T}$$

with $\alpha = 2.0 - 3.5\ (\mathrm{GeV}/c)^{-1}$, $\beta > 3.0$

which yield cross-sections between 13-60 μb for $D\bar{D}$ production.

If we assume this distribution with the best fit parameters from Brown et al., $\alpha = 2.5$ and $\beta = 5.0$, and a semileptonic branching ratio of D's into muons of 10%, our data are consistent with a cross-section for $D\bar{D}$ production 20μb. The calculated contribution from $D\bar{D}$ is shown in figure 4-9. By varying the parameters of the model over the acceptable range the charm cross-section necessary to account for the muon yield at P_T=1.5 Gev/c varies from 20 to 30 μb. Using the B-G parameterization we obtain the same results.

For B production we assume the same range of production parameters(i.e. α=2.0-3.5(GeV/c)$^{-1}$, β>3.0) as used for D production, and a 10% branching ratio for B's into muons. The contribution from $B\bar{B}$ to the muon yield peaks at around P_T = 2GeV/c as seen in Fig. 4-10. The $B\bar{B}$ contribution shown in this plot was calculated to give an excess of 3 standard deviations over the data point at P_T=2.31 GeV/c when added to the other contributions(ψ and $D\bar{D}$ in this region). This required a $B\bar{B}$ production cross-section of 200 nb/nucleon, which implies an upper limit

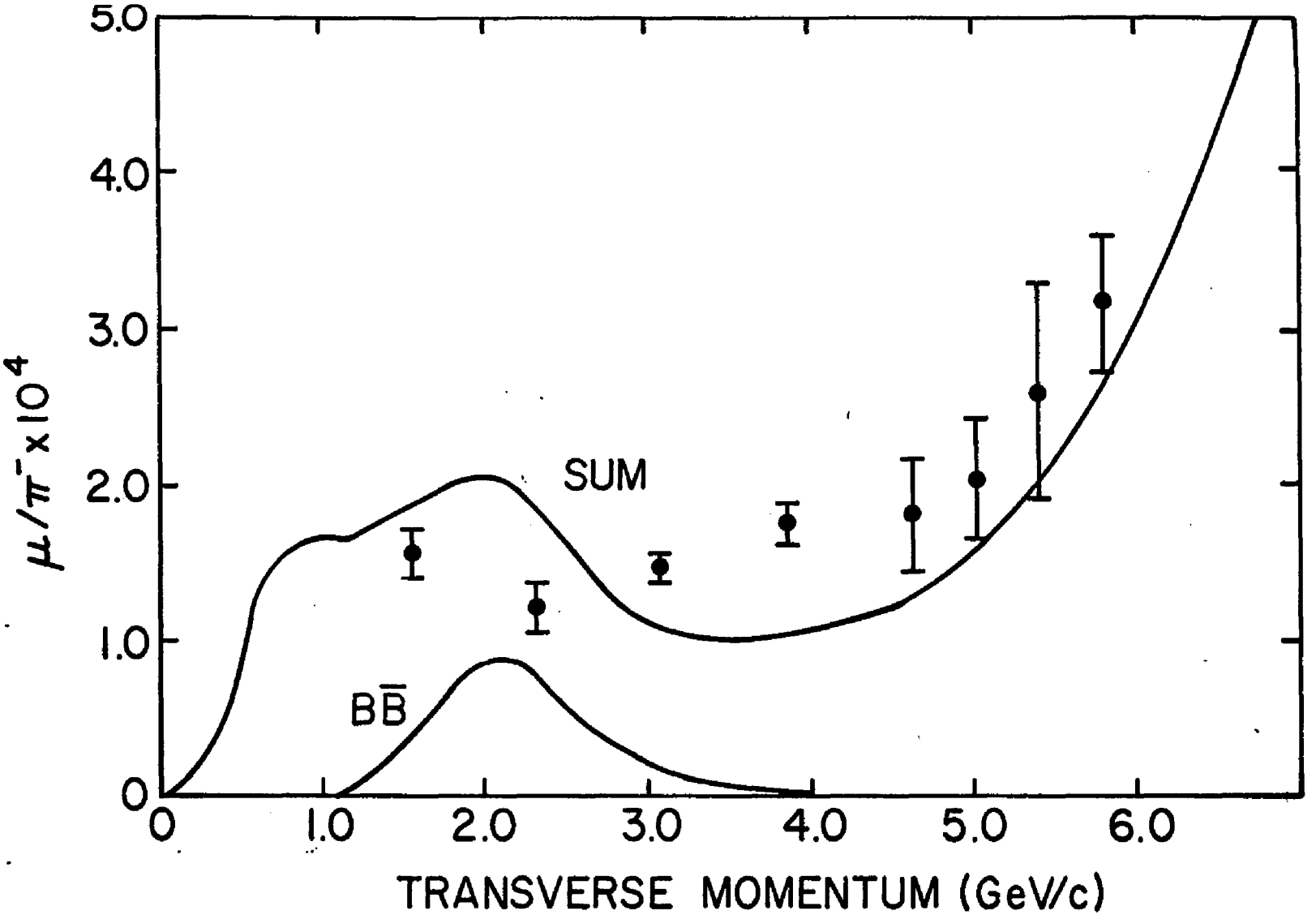

CONTRIBUTION OF $B\bar{B}$ TO CALCULATED SINGLE MUON YIELD ASSUMING A 200 nb. PRODUCTION CROSS-SECTION.

FIG. 4-10

for the production of $B\bar{B}$:

$$\sigma_{B\bar{B}} < 200 \text{ nb/nucleon}$$

Such a conservative limit was used because the contribution of the tail of the $D\bar{D}$ over this region can vary by a factor of 2 depending on the model parameters chosen. This upper bound is consistent with the 50 nb limit measured by A. Diamant-Berger et al.[22] for 400-GeV/c protons incident on a Fe target. Quantum chromodynamics calculations give estimates of approximately 10 nb for hadronic production of BB at these energies.

Electron-Muon Coincidences

The direct electron yield at p_T=4.62 GeV was measured to be:

$$\frac{e_{dir}}{\pi^-} = (2.45 \pm .45) \times 10^{-4}$$

No electron muon coincidence signal was observed above background. The measured ratio of electron-muon coincidences to single direct electrons was determined to be:

$$\frac{e\mu}{e_{dir}} = .0004 \pm .008 \quad ; \; p_T^e = 4.62$$

This is to be compared with the ratio of $\mu\mu$ coincidences to single direct muons:

$$\frac{\mu\mu}{\mu_{dir}} = .065 \pm .0095 \quad ; \; p_T^\mu = 4.62$$

This yields a 90% confidence level upper limit for the ratio of $e\mu/\mu\mu$:

$$\frac{e\mu}{\mu-\mu} < .27$$

SUMMARY

1. The ratio μ/π rises by a factor of 2 from p_T=1.5 GeV to p_T=6 GeV.

2. The inclusive cross-section for production of single muons increases linearly with the atomic number of the target.

3. Continuum dimuons contribute significantly to the single muon yield at p_T > 4 GeV.

4. To account for the large single muon yield in terms of known particles a significant contribution must arise from decays of the J/ψ for p_T between 3 and 6 GeV.

5. Assuming the majority of the single muon yield at P_T=1.5 GeV is from charm, the data are consistent with a $D\bar{D}$ production cross-section between 20 and 30 μb.

6. The single muon yield at low P_T imposes an upper bound of 200 nb on the production of $B\bar{B}$ in 300 GeV/c p-N interactions.

7. The bulk of the dimuon signal (> 60%) is not from a process which would produce e-μ pairs in the same quantity.

APPENDIX I

MATERIAL IN THE SPECTROMETER BEAM LINE

object	amount	ABSORPTION LENGTHS	RADIATION LENGTHS
A1+A2+A3	3 x .25" =.75" scintillator	.031	.045
H1+H2+H3+H4	8 x .0625=1.5" scintillator	.061	.091
CERENKOV MIRRORS	2 x .25" = .5" pyrex glass	.031	.105
CERENKOV WINDOWS	4 x .125"= .5" aluminum	.036	.14
LITTLE CERENKOV MIRROR	.0625" aluminum	.005	.02
LITTLE CERENKOV WINDOW	.03" aluminum	.002	.01

total loss in spectrometer---------- .166

total radiator thickness in beam line---------- .411

APPENDIX II

The corrected signal at each conversion length is given by the sum of the contributions discussed on page 65.

$$N_e(x) = N_{dir} + N_e^{\pi^o}(D_{\pi^o} + x) + N_e^{\eta} \ (D_{\eta} + x) \qquad (II.1)$$

$$= N_{dir} + N_e^{\pi^o} D_{\pi^o} + N_e^{\eta} \ D_{\eta} + (N_e^{\eta} + N_e^{\pi^o}) \ x$$

$N_e(x)$ = corrected yield of electrons measured with x conversion lengths of material.

N_{dir} = Direct electron yield

$N_e^{\pi^o}$ = Electron yield from π^o/conversion length

N_e^{η} = Electron yield from η/conversion length

D_{π^o} = Dalitz pair equivalent conversion length

= 5.83×10^{-3}

D_{η} = Dalitz pair equivalent conversion length

= 8.1×10^{-3}

x = Amount of radiator present, measured in conversion lengths

= $\frac{7}{9}\frac{L}{x_o}$, where x_o = radiation length

η production was measured by Busser et al.[19] with the result

$$\frac{N_{\eta}}{N_{\pi^o}} = .55$$

Since the energy of the parent particle is very high compared with its mass we approximate

$$\frac{N_e^{\eta}}{N_e^{\pi^o}} = \frac{N_{\eta}}{N_{\pi^o}} \ \frac{\Gamma(\eta \to \gamma\gamma)}{\Gamma(\pi^o \to \gamma\gamma)} = .209 \pm .038 = A$$

Substituting into (II.1) above:

$$N_e(x) = N_{dir} + N_e^{\pi^o} \ (D_{\pi^o} + A \ D_{\eta} + (1+A) \ x) \qquad (II.2)$$

N_{dir} can then be obtained by extrapolating to a negative conversion length given by:

$$D_{\pi^o} + A\, D_\eta + (1+A)\, x = 0$$

$$x_o = -\frac{D_{\pi^o} + A\, D_\eta}{1+A} = -6.22 \times 10^{-3}$$

The result we obtain is best stated as a ratio of the electron to pion yields.

$$\frac{N_e(x)}{N_\pi} = \frac{N_{dir}}{N_{\pi^-}} + \frac{N_e^{\pi^o}}{N_{\pi^-}} (D_{\pi^o} + D_\eta) + (1+A) \frac{N_e^{\pi^o}}{N_{\pi^-}} x \qquad (II.3)$$

A graphical representation of the extrpolation is shown in figure 3-13 employing the corrected electron yields at each conversion length. The predicted slope shown is obtained from equation (II.3):

$$S = (1+A) \frac{N_e^{\pi^o}}{N_{\pi^-}} = (1+A) \frac{N_{\pi^o}}{N_{\pi^-}} \frac{N_e^{\pi^o}}{N_{\pi^o}} = (118.3 \pm 7.7) \times 10^{-4}$$

arrives

$$\frac{N_{\pi^o}}{N_\pi} \simeq \frac{\frac{1}{2}(N_{\pi^+} + N_{\pi^-})}{N_{\pi^-}} = 1.07 \pm .06$$

where the π^+ and π^- yields were measured in this apparatus.

REFERENCES

[1] L. Kluberg et al., Phys. Rev. Lett. 31,1426(1973).

[2] D. Antreasyan, Ph.D. Thesis, University of Chicago(1978).

[3] R Burns et al., Phys. Rev. Lett. 15,830(1965).

[4] R.C. Lamb et al., Phys. Rev. Lett. 15,800,(1965).

[5] Y. Yamaguchi, Nuovo Cimento 43,193,(1966).

[6] J.H. Christenson et al., Phys. Rev. D8,2016(1973).

[7] C.B. Bonderenko et al., Proceedings of the XVITh International Conference on High Energy Physics,Chicago-Batavia, p.329(1973).

[8] J.P. Boymond et al., Phys. Rev. Lett. 33,112,(1974).

[9] J.A. Appel et al., Phys. Rev. Lett. 33,722(1974).

[10] F.W. Busser et al., Phys. Lett. 53B,212(1974).

[11] S.D. Drell and T.M. Yan, Phys. Rev. Lett. 25,316(1970).

[12] M. Bourquin and J.M. Gaillard, Nucl. Phys. B114,334(1976).

[13] K.W. Brown et al., Phys. Rev. Lett. 43,410(1979).

[14] J.J. Aubert et al., Phys. Rev. Lett. 33,1404(1974).

[15] D. Antreasyan et al., Phys. Rev. Lett. 39,906(1977).

[16] L.M. Lederman, Proceedings of the XIXth International Conference on High Energy Physics,Tokyo(1978).

[17] D. Antreasyan et al., Phys. Rev. Lett. 39,906(1977).

[18] F.W. Busser et al., Nucl. Phys. B113,189(1976).

[19] H.D. Snyder et al., Phys. Rev. Lett. 36,1415(1976).

[20] J.K. Yoh et al., Phys. Rev. Lett. 38,684(1978).

[21] J.G. Branson et al., Phys. Rev. Lett. 38,1334(1977).

[22] Ueno et al., Phys. Rev. Lett. 42,4869(1979).

[24] A. Diamant-Berger et al., Phys. Rev. Lett. 44,507(1980).